Cell Reports
Volume 42
Number 5
May 30, 2023

CellPress

Cell Reports

Resource

An anatomical and connectivity atlas of the marmoset cerebellum

Graphical abstract

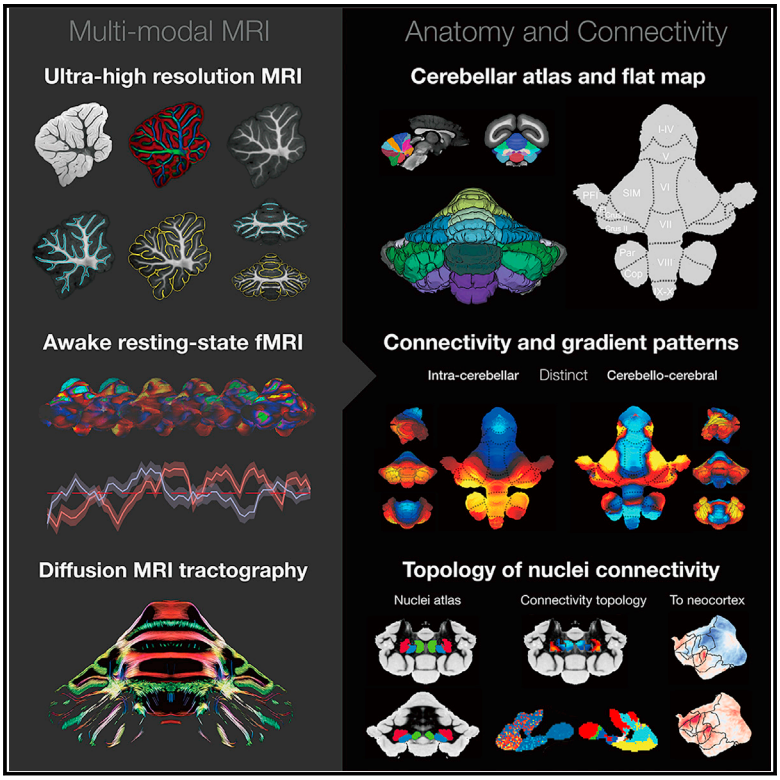

Highlights

- Detailed anatomical atlases and surfaces of the cerebellum based on ultra-high-resolution MRI
- Distinct patterns of the intra-cerebellar and the cerebello-cerebral functional gradients
- Functional connectivity patterns between the cerebellar cortex and the functional networks
- Connectivity topology of the cerebellar nuclei to the cerebellar cortex and the neocortex

Authors

Xiaojia Zhu, Haotian Yan, Yafeng Zhan, Furui Feng, Chuanyao Wei, Yong-Gang Yao, Cirong Liu

Correspondence

yaoyg@mail.kiz.ac.cn (Y.-G.Y.), crliu@ion.ac.cn (C.L.)

In brief

Zhu et al. present a marmoset cerebellum atlas, revealing anatomical details, functional connectivity patterns, and cerebellar nuclei topological relationships in cerebello-cerebral circuits. Using ultra-high-resolution *ex vivo* MRI and awake resting-state fMRI, this study provides resources and atlas tools to advance understanding of cerebello-cerebral circuits in non-human primates.

Zhu et al., 2023, Cell Reports *42*, 112480
May 30, 2023
https://doi.org/10.1016/j.celrep.2023.112480

CellPress

Cell Reports

CellPress
OPEN ACCESS

Resource

An anatomical and connectivity atlas of the marmoset cerebellum

Xiaojia Zhu,[1,2,3] Haotian Yan,[2] Yafeng Zhan,[2] Furui Feng,[2] Chuanyao Wei,[2,3] Yong-Gang Yao,[1,3,*] and Cirong Liu[2,3,4,5,*]
[1]Key Laboratory of Animal Models and Human Disease Mechanisms of the Chinese Academy of Sciences and Yunnan Province, and KIZ-CUHK Joint Laboratory of Bioresources and Molecular Research in Common Diseases, National Research Facility for Phenotypic & Genetic Analysis of Model Animals (Primate Facility), National Resource Center for Non-Human Primates, Kunming Institute of Zoology, Chinese Academy of Sciences, Kunming 650201, China
[2]Institute of Neuroscience, CAS Center for Excellence in Brain Science and Intelligence Technology, CAS Key Laboratory of Primate Neurobiology, State Key Laboratory of Neuroscience, Chinese Academy of Sciences, Shanghai 200031, China
[3]University of Chinese Academy of Sciences, Beijing 100049, China
[4]Shanghai Center for Brain Science and Brain-Inspired Intelligence Technology, Shanghai, China
[5]Lead contact
*Correspondence: yaoyg@mail.kiz.ac.cn (Y.-G.Y.), crliu@ion.ac.cn (C.L.)
https://doi.org/10.1016/j.celrep.2023.112480

SUMMARY

The cerebellum is essential for motor control and cognitive functioning, engaging in bidirectional communication with the cerebral cortex. The common marmoset, a small non-human primate, offers unique advantages for studying cerebello-cerebral circuits. However, the marmoset cerebellum is not well described in published resources. In this study, we present a comprehensive atlas of the marmoset cerebellum comprising (1) fine-detailed anatomical atlases and surface-analysis tools of the cerebellar cortex based on ultra-high-resolution *ex vivo* MRI, (2) functional connectivity and gradient patterns of the cerebellar cortex revealed by awake resting-state fMRI, and (3) structural-connectivity mapping of cerebellar nuclei using high-resolution diffusion MRI tractography. The atlas elucidates the anatomical details of the marmoset cerebellum, reveals distinct gradient patterns of intra-cerebellar and cerebello-cerebral functional connectivity, and maps the topological relationship of cerebellar nuclei in cerebello-cerebral circuits. As version 5 of the Marmoset Brain Mapping project, this atlas is publicly available at https://marmosetbrainmapping.org/MBMv5.html.

INTRODUCTION

The common marmoset has risen quickly as a promising non-human primate (NHP) model for neuroscience research.[1–3] Due to its small brain size, the marmoset provides advantages in the study of brain anatomy and the functional mapping of brain architecture, all of which has enabled the development of valuable open resources and research tools.[4–11] Specifically, via the Marmoset Brain Mapping project (https://marmosetbrainmapping.org), we have provided ultra-high-resolution *ex vivo* diffusion MRI and awake resting-state fMRI data of the marmoset brain.[12–15] Based on the resource, we have produced an anatomical and functional atlas of the marmoset cerebral cortex in fine detail and created useful templates for surface-based visualization and analysis. Together with the Marmoset Brain Connectivity project,[15–17] a neuronal tracing database of the marmoset neocortex, our resources greatly facilitate the study of the neuroanatomy and the connectome of the marmoset brain.[18]

Despite the recent progress and the public availability of the resources, one of the major brain regions, the cerebellum, has only been described in histological atlas books, including the Paxinos atlas[19] and the Hardman atlas,[20] but has not been mapped in the earlier published digital atlases for imaging and connectome studies. The cerebellum, historically regarded as a motor-control region, is now found to be a critical node in neural circuits involved in a wide range of cognitive functions.[21–24] These functions involve bidirectional communication between the neocortex and the cerebellum.[24] In particular, recent studies used diffusion embedding, a non-linear dimensional reduction method, to obtain the gradients in the similarity matrices of the resting-state fMRI functional connectivity (functional gradient) of the cerebellar cortex.[25,26] These gradients reflected spatial distribution patterns of the variances in the functional connectivity of the cerebellar cortex and were associated with distinct brain networks and diverse task domains.[22,25,27] Although the cerebellar cortex has a remarkably uniform cytoarchitecture and stereotypic local circuitry, it shows a rich diversity of region-specific connectivity to the neocortex, the description of which is essential to the understanding of the functional dynamics and the neural circuits that underlie motor-control and cognitive functioning.[28,29]

In the current study, we have aimed to develop a comprehensive atlas of the marmoset cerebellum by using the multi-modal MRI data of the Marmoset Brain Mapping project (https://marmosetbrainmapping.org). First, based on our ultra-high-resolution *ex vivo* MRI, we developed an anatomical atlas of the cerebellar cortex and high-resolution surfaces that preserved fine-grained folia patterns. Second, using our recently released

resources of awake resting-state fMRI,[15] we examined the functional connectivity patterns of the cerebellum and compared the gradient patterns of the intra-cerebellar and the cerebello-cerebral functional connectivity. Last, based on diffusion tractography and functional connectivity analysis, we performed connectivity-based mapping of the cerebellar nuclei, which reflected nucleus-specific connectivity patterns in cerebellar-cerebral circuits. The cerebellar atlases can be downloaded for data analysis or interactively viewed online, utilizing the web-based atlas viewer of the Marmoset Brain Mapping Project (https://marmosetbrainmapping.org/MBMv5.html). The study greatly extends the available neuroimaging resources of the marmoset brain and will accelerate comparative studies of the cerebellum.

RESULTS

Fine-detailed surface reconstruction and lobular parcellations of the cerebellar cortex

We constructed a fine-grained surface and lobular parcellation of the marmoset cerebellar cortex based on ultra-high-resolution *ex vivo* MRI data.[13] Although the marmoset has an almost smooth neocortex, its cerebellar cortex is tightly folded into a complex folia pattern (Figure 1). As the cerebellar cortex is a thin and folded sheet of neuronal tissue, a folium of the marmoset is hard to resolve by normal *in vivo* MRI due to the partial volume effects (Figure 1A and 1B). Thus, *ex vivo* MRI with ultra-high resolution becomes essential to describe the detailed 3D folding patterns of the cerebellar cortex. As shown Figure 1, our ultra-high-resolution MRI data[13] were able to resolve the detailed pattern of an individual folium and the structure of its layers.

Based on the ultra-high-resolution data, we manually segmented the cerebellum into gray matter and white matter (Figure 1D) and then reconstructed the folia-level pial and white matter surfaces using Freesurfer[30] (Figures 1E and 1F). As the pial surface was expanded from the white matter surface, the vertices were paired and matched on the two surfaces. To show the hierarchical levels of folding patterns from large lobules to small folia, the surfaces were densely tessellated with a total of 286,308 vertices and 572,724 faces. As the detailed folding patterns complicated the visualization of the cerebellar data, we unfolded the pial surface and created the flat maps of the marmoset cerebellar cortex (Figure 1G). The flat map was built on dense tessellated surfaces, which were unfolded down to the level of the individual folium. The dense tessellated flat map fully took advantage of the high-resolution MRI data to preserve the anatomical details of the cerebellar cortex.

We manually delineated the cerebellar lobules on the ultra-high-resolution templates according to the nomenclature of the Paxinos atlas.[19] The cerebellar cortex was parcellated into the 17 lobules: lingula I (I), central lobule II (II), culmen III (III), declive IV (IV), lobule V (V), folium VI (VI), tuber VII (VII), pyramid VIII (VIII), uvula IX (IX), nodulus X (X), simplex lobule (SIM), paramedian lobule (Par), copula (Cop), flocculus (Fl), paraflocculus (PFl), Crus I, and Crus II (Figure 2A). For convention, we merged lobules I, II, III, and IV into one region (I–IV) and IX and X into the vestibulocerebellar region (IX–X) to form a 13-lobule parcellation (Figures 2A–2C), following a similar strategy as described in a study for the human cerebellar atlas.[31] The anatomical lobular atlas was mapped onto the surfaces and the flat map to facilitate surface-based analysis (Figure 2D).

The high-resolution volumetric and surface atlases allowed us to accurately estimate the volume and surface area of the whole cerebellar cortex and each lobule. After applying a brain-shrinkage correction (see STAR Methods), the total volume and area of the cerebellar cortex are 838.3 and 1,782.8 mm^2 at an 80-μm isotropic resolution, respectively (Figures 2E; Table 1). Note that we also estimated the surface area at a higher resolution (a 50-μm isotropic T2* structural image) and obtained a surface area of 1,812.7 mm^2, close to the estimation based on 80-μm multi-modal data. The result suggests that the 80-μm resolution was sufficient to distinguish most individual folia. The three largest lobules are PFl, SIM, and lobule V, and the three smallest lobules are lobule I, Fl, and lobule II (note: the flat map did not reflect the surface area of the lobules due to the surface flattening). We also measured the surface area of each lobule on the downsampled data (Figure 2E, right). For the lower resolution in which the folia failed to be fully reconstructed, the surface area was largely underestimated. For example, we downsampled our data into 150-μm isotropic, 250-μm isotropic (typical *in vivo* structural data of the marmoset brain), and 500-μm isotropic (typical *in vivo* diffusion MRI data), and their estimated surface areas were reduced to 1,383 (77.6% of the original size), 1,124.2 (63.1%), and 730.4 mm^2 (41%), respectively (Figure 2E; Table S1). Thus, the high resolution was essential to reveal the folia pattern and estimate the accurate area size of the cerebellar cortex.[32]

Distinct functional gradients of the intra-cerebellar connectivity and the cerebello-cerebral connectivity

Previous human studies have revealed that the cerebellar cortex shows distinct topographic patterns of intrinsic functional connectivity more relevant to its functional domains than to the anatomical lobular parcellations.[22,25] To reveal the functional connectivity pattern of the marmoset cerebellar cortex, we calculated the functional gradients by analyzing the intra-cerebellar functional connectivity and the cerebello-cerebral connectivity using diffusion map embedding.[27,33,34]

We first examined the principal gradients (gradient 1), which accounted for the largest part of the variability in the resting-state connectivity patterns (Figure S1A). For gradient 1 of the intra-cerebellar functional connectivity (Figure 3A), the negative extreme (blue) was in areas of motor representation (lobules I–VI) and gradually extended to areas of non-motor representation with the positive extreme (orange) located in Crus I–II and Par. The gradient 1 of the cerebello-cerebral connectivity was more complex and had one extreme in cerebellar vermis and lobules I–VI, which extended to Crus I and Crus II and reached the Sim and PFl as the other extreme. Other gradients of the intra-cerebellar and cerebello-cerebral functional connectivity also showed different patterns in different lobules (Figure 3A). For example, gradients 2 and 3 of the intra-cerebellar connectivity were asymmetrical, with their positive extremes located in the lobules VI and Crus I–II, respectively. On the contrary, gradients 2 and 3 of the cerebello-cerebral connectivity were symmetrical with more complex gradient-changing patterns. We quantitatively analyzed the spatial relationship between the intra-cerebellar and the cerebello-cerebral

CellPress
OPEN ACCESS

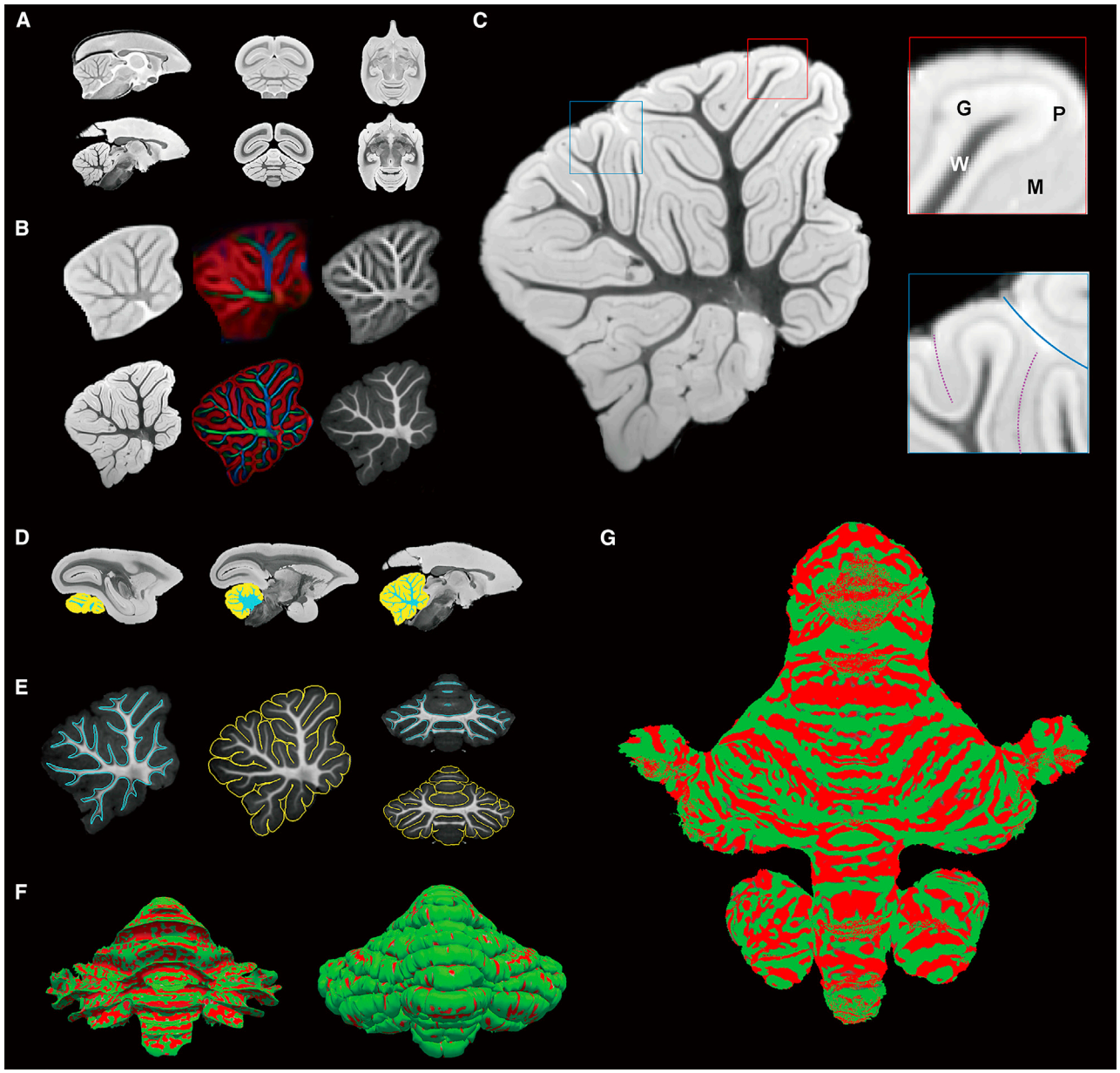

Figure 1. Ultra-high-resolution *ex vivo* MRI reveals anatomical details of the marmoset cerebellum

(A) The top is the *in vivo* 200-μm T2-weighted population template, and the bottom is the *ex vivo* 50-μm T2*-weighted image.

(B) The middle-sagittal slice of the cerebellum. The top shows the T2-weighted, diffusion tensor-based directionally encoded color (DEC), and the T1-weighted images (from left to right) of the *in vivo* 200-μm images. The bottom displays the T2*-weighted, DEC image and the magnetization transfer ratio (MTR; T1-weight-like contrast) of the *ex vivo* 80-μm images.

(C) The zoomed-in view of a middle sagittal slice of the cerebellum. Our ultra-high-resolution *ex vivo* image reveals the layer pattern (an example highlighted in the red box) and the folia pattern (highlighted in the blue box). W, white matter; G, granular layer; P, Purkinje layer; M, molecular layer. Blue solid line: big lobular boundary; purple dash lines: boundaries of small folia.

(D) The segmentation of the cerebellum into white matter (blue) and gray matter (yellow). From left to right shows sagittal slices of the T2*-weighted image.

(E) The surface outlines are displayed on the *ex vivo* MTR image. A middle sagittal slice and a coronal slice show the white matter surface outline in blue and the pial surface in yellow.

(F) The 3D view of the white matter surface (left) and the pial surface (right). The curvature of the cortex is displayed as the overlay.

(G) Flat map of the cerebellar cortex, generated from the surface displayed in (E). Colored overlay shows the curvature of the cortex, with gyri in green and sulci in red.

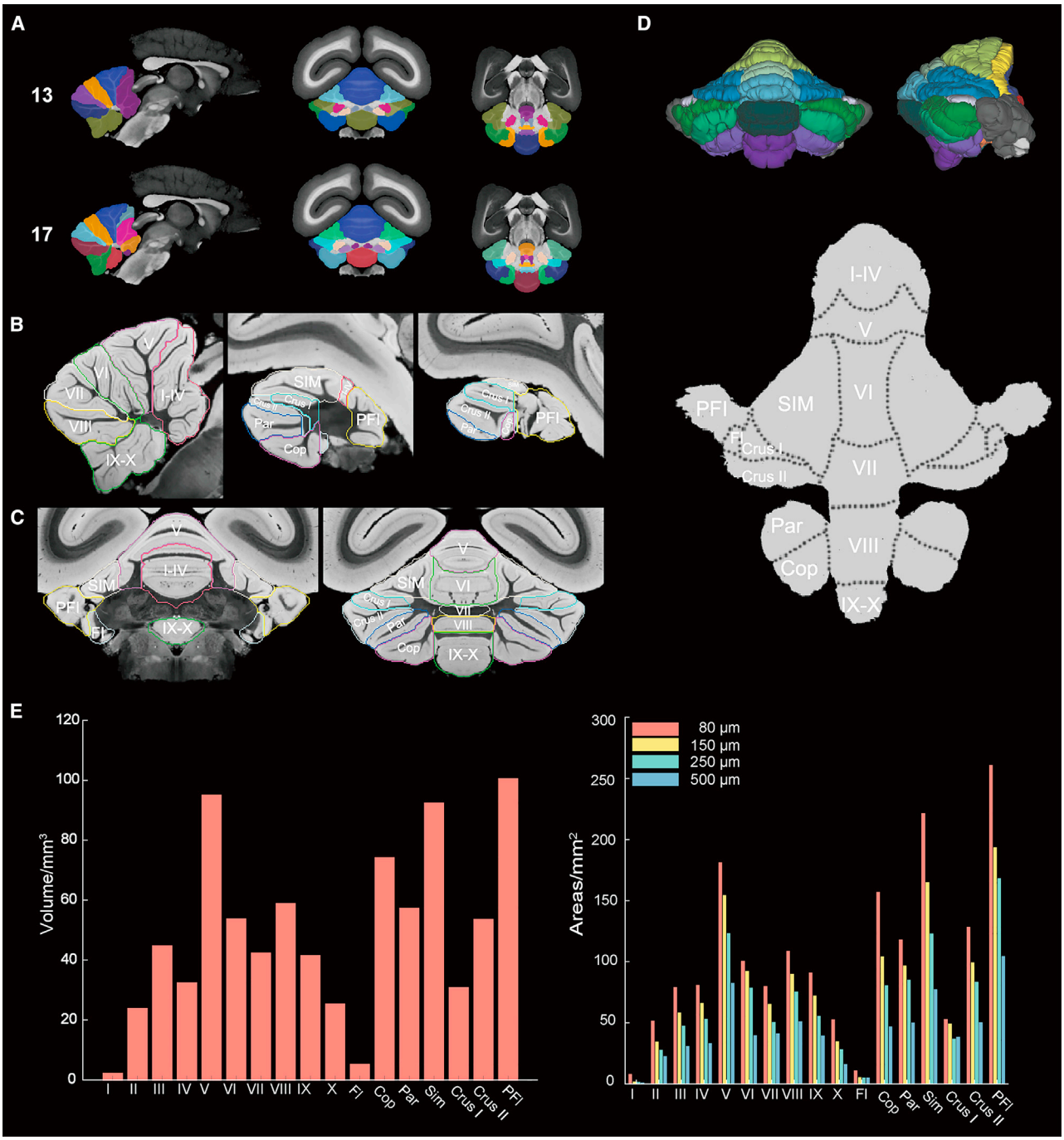

Figure 2. The lobular parcellation of the cerebellar cortex

(A) The atlas of lobular parcellation. The top is the 13-lobular parcellation and the bottom is the 17-lobular parcellation. From left and right are examples of sagittal, coronal, and horizontal slices. The underlying image is an *ex vivo* MTR image.

(B) Examples of three sagittal slices of the 13-lobular parcellation on an *ex vivo* T2*-weighted image.

(C) Examples of two coronal slices. The 13 lobules include I–IV, V, VI, VII, VIII, IX–X, SIM, Par, Cop, Fl, PFI, Crus I, and Crus II.

(D) The 13-lobular parcellation on the surface (top panel) and flat map of the cerebral cortex (bottom panel).

(E) The volume size of the 17 cerebellar lobules (left) and the estimated surface areas using data with different resolutions (right). Detailed values of sizes are provided in Tables 1 and S1.

Table 1. The volume and surface area of 17 lobules

Lobules	I	II	III	IV	V	VI	VII	VIII	IX
Volume/mm^3	2.44	24.03	45.04	32.63	95.27	54.06	42.57	59.07	41.74
Area/mm^2	8.04	51.49	79.09	80.88	181.25	100.72	79.98	108.58	90.94
Lobules	X	SIM	Par	Cop	Fl	PFl	Crus I	Crus II	Total
Volume/mm^3	25.52	92.66	57.53	74.45	5.49	100.76	31.10	53.84	838.30
Area/mm^2	52.58	221.35	118.06	156.76	10.97	260.86	52.92	128.26	1782.80

Note: the 17 lobules in the marmoset cerebellar cortex are parcellated following the nomenclature of the Paxinos atlas,[19] and the volumes are estimated from ultra-high-resolution *ex vivo* data of one marmoset.[13]

gradients in both marmosets and humans. The analysis revealed differences between the two species in terms of the similarity of these gradients (Figure 3B). In humans, the first four gradients of both types demonstrated high similarity, with the first two gradients being nearly identical (with R values exceeding 0.9), indicating a strong influence of cerebello-cerebral connections on intra-cerebellar connectivity.[25] In contrast, the results for marmosets exhibited weaker relationships between the two types of gradients. The percentage of data variance explained by the two types of gradients was also similar in humans but not in marmosets (Figure S1). Furthermore, in marmosets, the fourth intra-cerebellar gradient (4.75% of variance) demonstrated weak similarity (with an R value of 0.62) to the first cerebello-cerebral gradient (35.19% of variance). The third intra-cerebellar gradient (5.57% of variance) displayed weak similarity (with an R value of 0.6) to the fourth cerebello-cerebral gradient (3.11% of variance). While these similarities in marmoset gradient patterns are weaker than those observed in humans, they suggest that the influence of cerebello-cerebral connections on the intrinsic functional connectivity of the cerebellar cortex also exists in marmosets, albeit to a much lesser extent. These results highlight the evolutionary divergence in the functional connectivity between the neocortex and cerebellar cortex in the two primate species examined.

Due to the large individual variability in the functional connectivity of marmoset brains, the population-level functional gradients may not capture the individual functional connectivity patterns of the cerebellum. Based on awake resting-state fMRI of 39 marmosets, we examined the individual variability of both the intra-cerebellar and the cerebello-cerebral principal gradients (Figures 3C and S2). For both types of gradients, their two extremes had the lowest individual-level variability (the darkest areas), while the areas with the highest variabilities were mainly located at the boundary of two extremes. The result indicated that the functional connectivity patterns in the gradient extremes were highly consistent across individuals and that the variability increased gradually from two extremes to other areas.

To characterize the spatial distribution of the gradient extremes, we mapped the top 10% values of gradient 1, the top 10% values of gradient 2, and the lowest 10% values of gradient 1 (Figure 4, left) on lobular parcellations. For the intra-cerebellar gradients (Figure 4A), the top 10% values were exclusively located at the non-motor lobules, including VII–X, FI, PFI, Cop, PM, Sim, Crus I, and Crus II, and the lowest 10% values were in motor areas, including lobules I–VI. The patterns were also reflected by spectral clustering on intra-cerebellar functional connectivity (Figure S3). In other words, the two extremes of the intra-cerebellar gradients were exclusively located in either non-motor or motor areas. On the contrary, the top values of the cerebello-cerebral gradients were in both the motor and non-motor areas (Figure 4B), further indicating the differences between the two types of gradients.

The above gradient analyses showed the topological patterns of the cerebello-cerebral functional connectivity but did not demonstrate which cerebral regions connected with the cerebellum. In our previous studies, we provided a comprehensive mapping of the functional networks of the marmoset cerebral cortex.[15] Here, we calculated the functional connectivity of each cerebellar vertex to these cerebral networks to obtain the cerebellar connectivity maps of each network (Figures 5 and S4). Interestingly, the top extremes of cerebello-cerebral gradient 1 shown in Figure 4B were also the cerebellar areas that had the highest connectivity to most cerebral networks (Figure 5A), highlighting the importance of these areas for cerebello-cerebral communications. To verify the pattern, we calculated the variation of correlations to all fifteen networks that were defined in our recent study[15] for each cerebellar vertex and obtained a map of variation (Figure 5B), where low values represented consistent connectivity across different networks, and vice versa. The top extremes of cerebello-cerebral gradient 1 demonstrated the relatively strong and robust functional connectivity to most of the cortical networks compared with the other areas according to the variation map. The map showed a similar spatial pattern to gradient 1 of the cerebello-cerebral connectivity but not to that of the intra-cerebellar connectivity, indicating the divergence of the two types of functional connectivity of the cerebellar cortex.

Interestingly, in marmosets, the frontoparietal network and the default mode network exhibit a significant overlap in terms of cerebellar connectivity (R = 0.98), despite being spatially separated in the cortex. Using a winner-takes-all approach, we mapped the main network topological relationships, including somatomotor, premotor, frontoparietal, and default mode networks, to the cerebellar cortex (Figure 5C). We found that the default network and the frontoparietal network occupied adjacent but distinct zones in the non-motor areas of the cerebellar cortex, which is consistent with previous reports in humans.[36] We further analyzed the functional connectivity between the cerebellar cortex and the seven cerebral networks of humans[35] (Figure 5D). Compared with marmosets, the frontoparietal network and the default mode network in humans had a lower similarity, although they remained similar (R = 0.70), suggesting

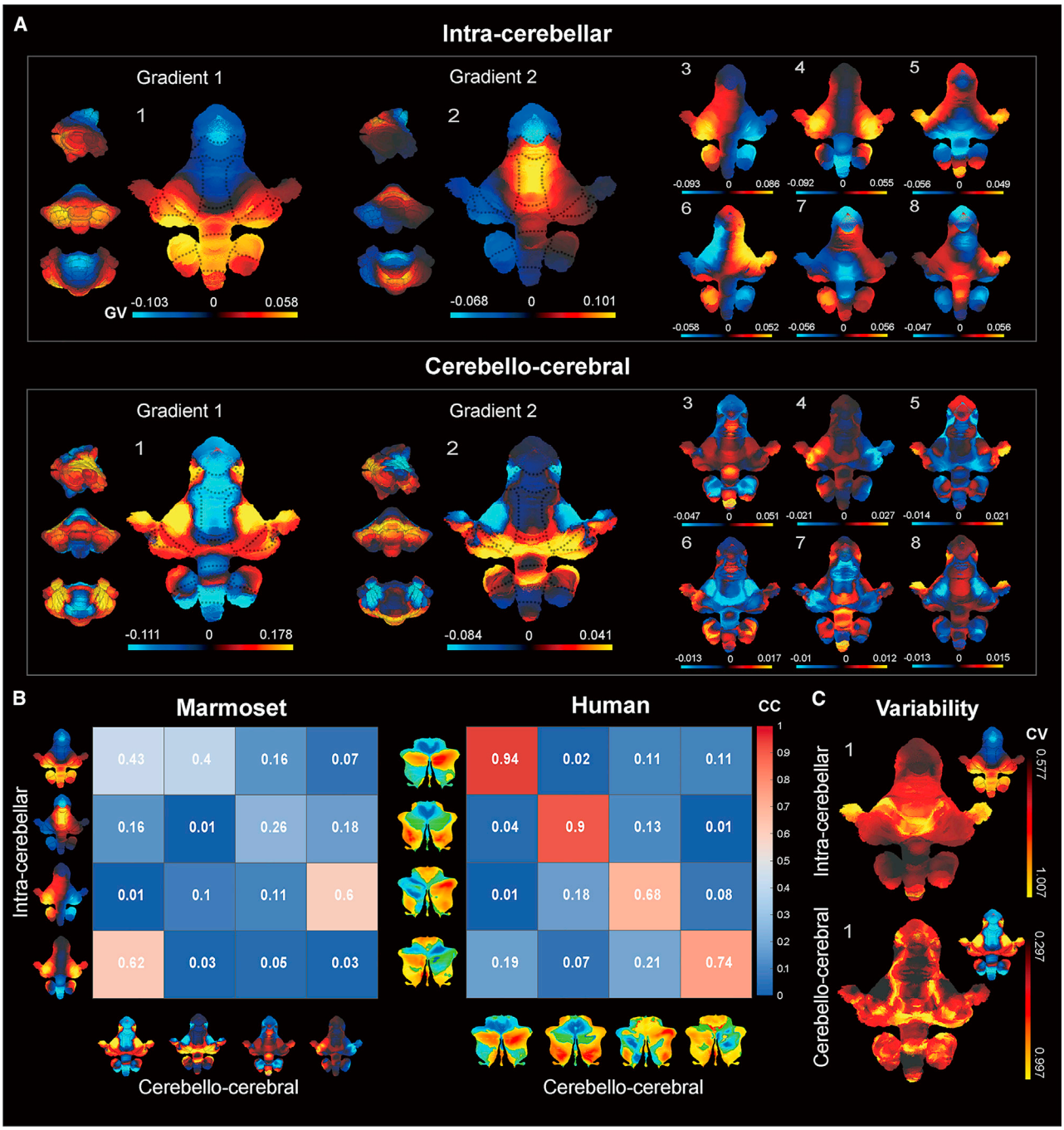

Figure 3. Functional gradients of the intra-cerebellar and the cerebello-cerebral connectivity

(A) Gradients 1 to 8 of the two types of connectivity. GV, gradient value.

(B) The corresponding gradients of the two types show similar spatial patterns in humans (right) but not in marmosets (left). The numbers and color are correlation coefficients (CCs) between the spatial patterns of two gradients.

(C) The individual variability of intra-cerebellar gradient 1 (top) and cerebello-cerebral gradient 1 (bottom); the color bar represents coefficients of variability (CVs). The gradient itself is also displayed on the right corner of each panel. The variabilities of other gradients (2–8) are displayed in Figure S2.

that the two networks may have diverged during primate evolution and become more distinguishable to the cerebellum in humans. Additionally, compared with marmosets, the functional connectivity between the cerebellum and the cerebral cortex was stronger in humans, supporting the notion that the intra-cerebellar gradients and the cerebello-cerebral gradients are more similar in humans due to stronger connections between the cerebral cortex and cerebellar cortex.

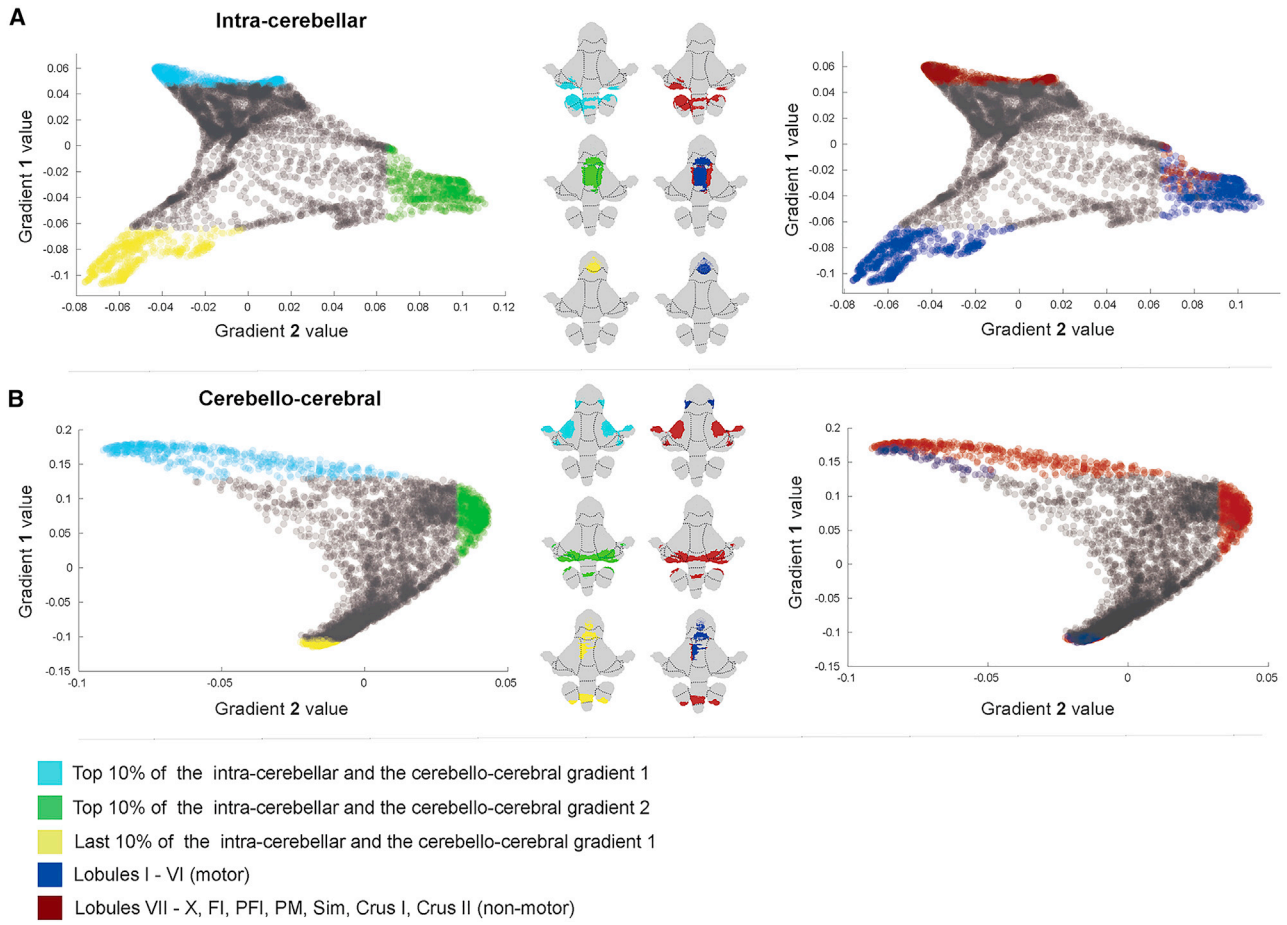

Figure 4. The spatial distributions of gradient extremes

(A and B) Scatter maps and regional distributions of the gradient extremes in the first two intra-cerebellar functional gradients (A) and the cerebello-cerebral functional gradients (B).

Structural-connectivity-based mapping reveals two extremes of the cerebellar nuclei in cerebello-cerebral circuits

In addition to the cerebellar cortex, cerebellar nuclei are the other substructures of the cerebellum. They are, from lateral to medial, the dentate nucleus, the interposed nucleus, and the fastigial nucleus. To characterize these nuclei, we constructed a 3D atlas on our high-resolution *ex vivo* templates and estimated their volumes (Figures 6A and 6B). The dentate nucleus was the largest, and its volume (13.72 mm^3) was more than the other two nuclei combined (interposed nucleus: 5.53 mm^3; fastigial nucleus: 5.28 mm^3). The size ratio of the dentate nucleus in the marmoset was higher than in the mouse but was similar to that of the rhesus monkey (Figure 6C), demonstrating the enlargement of the dentate nucleus in primate brains.

The cerebellar nuclei route information from different parts of the cerebellar cortex to other brain regions. Little is known about the connection between the cerebellar nuclei and the cerebellar cortex in the marmoset brain. Based on diffusion tractography, we estimated the structural connectivity between the nuclei and the cerebellar cortex to obtain their connectivity profiles. We then used the profiles to associate each nucleus voxel with the most-connected voxel of the cerebellar cortex (Figure 6D). According to the relationship, we assigned each nucleus voxel with the properties of its associated cerebellar-cortical voxel, including the value of gradient 1 of the cerebello-cerebral functional connectivity and the labels of the lobule parcellation. The structural-connectivity-based mapping was performed on two *ex vivo* data: the 80-μm isotropic (Figure 6D) and the 150-μm isotropic (Figure S6). Both sets of data produced consistent results, but a higher spatial resolution (80 μm) generated a more fine-grained mapping.

Most voxels of the dentate nucleus were assigned with one extreme (high values) of the cerebello-cerebral functional gradients and mainly stemmed from non-motor areas of the cerebellar cortex (Figure 6D). On the contrary, the fastigial nucleus occupied the other extreme (low values) of the cerebello-cerebral gradients. The assignment of cerebellar lobules also confirmed the connectivity patterns between the cerebellar cortex and nuclei. The fastigial nucleus was only connected to the vermis regions (lobules I–X) of the cerebellar cortex for motor functions, while the interposed nucleus and the dentate nucleus connect to more hemispheric areas such as Sim, Crus I, and Crus II for

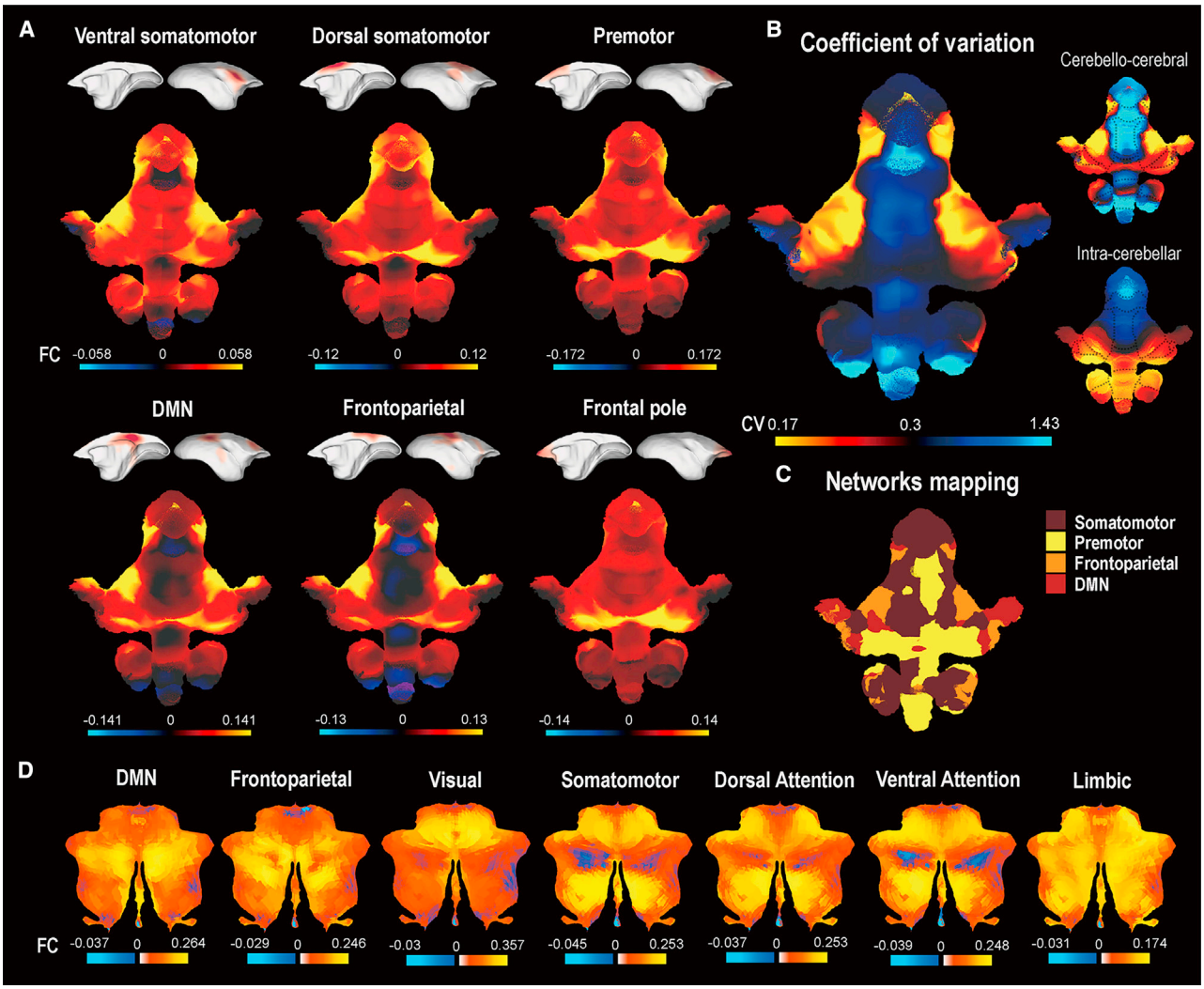

Figure 5. Functional connectivity patterns between the cerebral functional networks and the cerebellar cortex

(A) The functional connectivity between the cerebellar cortex and six selected cerebral networks. The connectivity maps to all cerebral networks are displayed in the Figure S4. The cerebral networks were defined by our previous study.[15] DMN, default model network.

(B) The variation map of the connectivity strengths to the cerebellar cortex across all cerebral networks (left). The map shows a similar spatial pattern as cerebello-cerebral functional gradient 1 (right-top) but differs from intra-cerebellar functional gradient 1 (bottom right).

(C) The cerebellar cortex parcellation was based on its connectivity to the cerebral cortex using a winner-takes-all approach.

(D) The functional connectivity between the cerebellar cortex and the seven cerebral networks[35] in humans, shown on the flat map of human cerebellar cortex.[31]

non-motor functions. This observation was consistent with the result seen in the mouse using anterograde virus tracing.[37] Overall, the structural-connectivity-based mapping revealed the topological relationship of the connections between the cerebellar cortex and the nuclei.

We then studied the topological relationship between the cerebellar nuclei and the cerebral cortex. As the projections from the cerebellar nuclei to the cerebral cortex are transsynaptic, diffusion tractography may not be able to reconstruct these indirect connections. Thus, we used the resting-state fMRI to map the cerebellar-nuclei-cerebral connections. We calculated the functional connectivity between the cerebellar nuclei and the cerebral cortex and analyzed their functional gradients. The principal gradient shows a clear continuous change from the dentate nucleus (highest extreme) to the fastigial nucleus (lowest extreme; Figure 6E), similar to the patterns in the structural-connectivity mapping of the cerebellar cortex (Figure 6D). To compare the functional connectivity patterns of the two extremes, we extracted the voxels with the top and the last 10% of the gradient and calculated their correlation strength to the cerebral cortex (Figures 6F and S7). The positive extreme (top 10%; mainly in the dentate nucleus) exhibited positive functional connectivity with most regions in the cerebral cortex, particularly in the motor and premotor cortical regions (MOTs), the dorsolateral prefrontal cortex (DLPFC), the medial prefrontal cortex (MPFC), the insular cortex (LS), and the auditory cortex

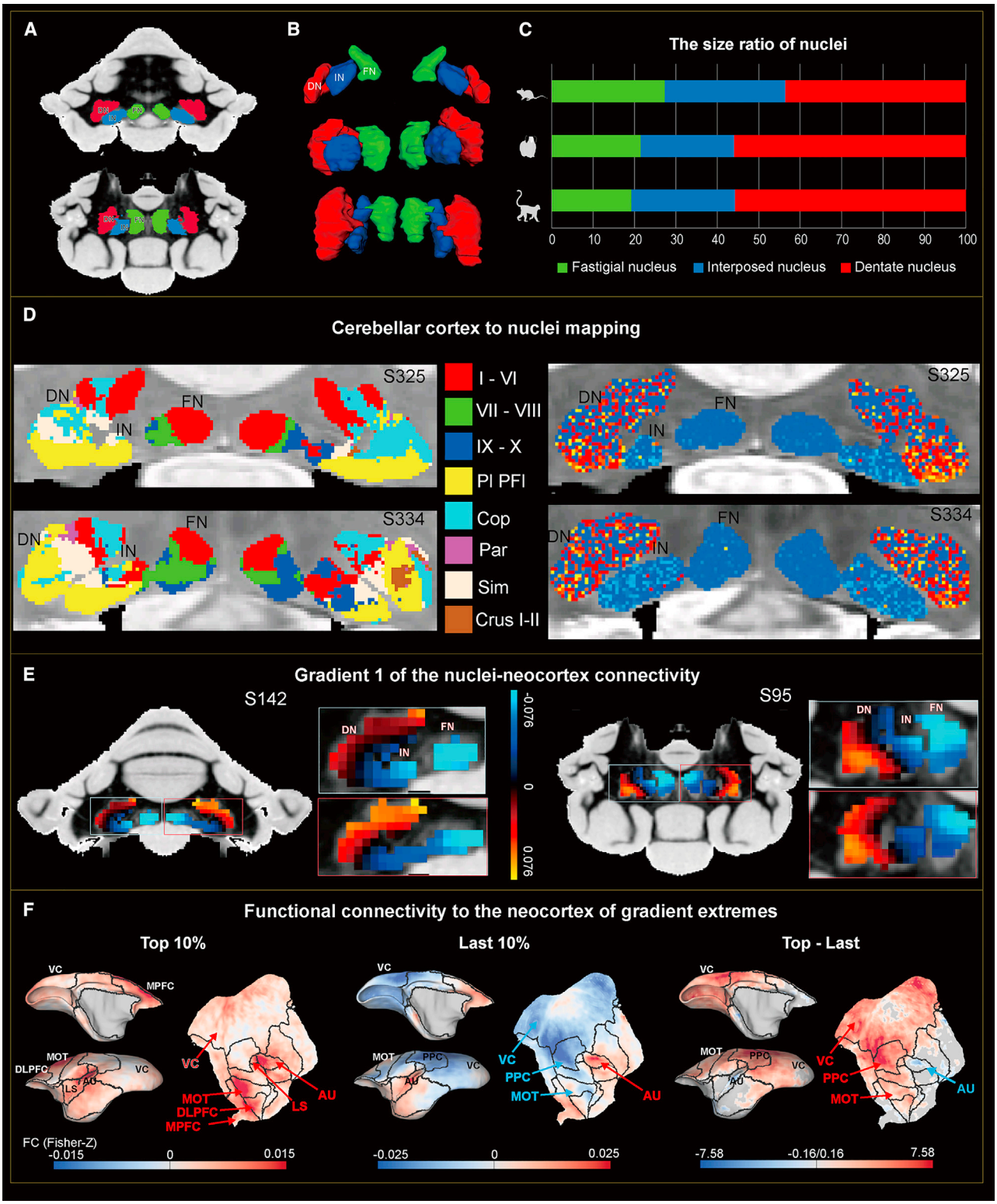

Figure 6. The structural-connectivity-based mapping and functional gradients of the cerebellar nuclei

(A) The anatomical atlas of the cerebellar nuclei of the marmoset. The top is a representative coronal slice, and the bottom is a horizontal slice. DN, dentate nucleus (red); IN, interposed nucleus (blue); FN, fastigial nucleus (green).

(B) The 3D view of the three cerebellar nuclei of the mouse (top), the marmoset (middle), and the macaque (bottom).

(legend continued on next page)

(AU). In contrast, the negative extreme (bottom 10%; mainly in the fastigial nucleus) displayed more negative functional connectivity with the cerebral cortex, such as the visual cortex (VC), the posterior parietal cortex (PPC), and the MOTs. A paired two-sample t test further confirmed the stronger functional connectivity of the dentate nucleus compared with that of the fastigial nucleus for most regions of the cerebral cortex, including the VC, the PPC, and the MOTs. The opposite connectivity patterns of the dentate nucleus and the fastigial nucleus indicated their distinct roles in the cerebello-cerebral circuit loop and cerebellar functions.

DISCUSSION

In the study, we developed a comprehensive atlas of the marmoset cerebellum based on ultra-high-resolution structural MRI data and awake resting-state fMRI data. This study has not only provided useful tools to facilitate neuroimaging and comparative studies of the primate cerebellum but also revealed anatomical and functional details of the marmoset cerebellum that were previously far from being well described.

The cerebellum and the neocortex co-evolved phylogenetically and expanded significantly in primate brains.[38–40] A previous study reported that the surface area of the human cerebellar cortex was equal to almost 80% of the total surface area of the neocortex but, in the macaque monkey, was approximately 33% of its neocortex,[32] which suggested that the cerebellum may play a prominent role in the evolution of human behaviors and cognition. Here, we measured the surface areas of the marmoset brain and found that the area of the cerebellar cortex was about 61.5% of that of the neocortex, which is lower than the ratio of humans (80%) but much higher than that of the macaque (33%). These surface areas of the cerebellar cortex suggested that a few species may not determine the co-evolutionary patterns between the cerebellum and the cerebral cortex, the size ratio of which may not be a simple linear relationship during evolution. Large-scale comparative neuroimaging across diverse species becomes essential to reveal the principles of cerebellar evolution and to examine the potential functional divergence.[41–44]

The gradient analysis can characterize functional connectivity patterns and reflect the anatomical and functional organization of the brain. The brain areas are not randomly organized but followed a center topographical organization. The topography, which shows roughly sensorimotor to *trans*-modal hierarchical changes, has been reported in brain cytoarchitecture, connectivity, and gene expression pattern.[33,45–48] The diffusion embedding method has proven useful for revealing the topographical pattern by recovering a low-dimensional spatial representation (functional gradients) from high-dimensional functional connectivity data.[27,33,34,49] Based on the diffusion embedding, our results and previous studies[25,26] revealed a similar functional gradient for the intra-cerebellar and the cerebello-cerebral functional connectivity of the human brain. The observation in humans suggested that the cerebello-cerebral connections may influence the intrinsic functional connectivity of cerebellar regions, which contributed to similar spatial distribution between the two types of gradients. In our study, we observed different gradient patterns of the intra-cerebellar and the cerebello-cerebral connectivity in the marmoset. Although the intra-cerebellar and the cerebello-cerebral principal gradients showed different patterns, both shared a similar topological spatial change with one extreme in areas related to motor functions and the other in the non-motor. The cerebello-cerebral principal gradient pattern also matched with the connectivity patterns of cerebral functional networks to the cerebellar cortex. These patterns demonstrated the influence of the cerebello-cerebral connections on shaping the functional connectivity pattern of the marmoset cerebellar cortex. However, these influences in the marmoset cerebellum may be not as strong as in humans, as we observed more complex gradient patterns of the cerebello-cerebral connectivity than that of the intra-cerebellar connectivity. The species difference indicates that the cerebellum and its connectivity with the cerebral cortex underwent prominent changes during primate evolution.

The cerebello-cerebral gradient reflected the functional connectivity patterns of different cerebellar networks to the cerebellar cortex in marmosets. One interesting observation was that the functional connectivity patterns of the frontoparietal-like and default-mode-like networks appeared to highly similar in the marmoset cerebellum (Figure 5). However, these networks were spatially distinguishable in both cerebral and cerebellar cortices in humans.[50] One major factor that may account for the discrepancy is the expansion of the prefrontal and parietal cortices in humans, resulting in more developed and well-separated networks for association cortices, including the default mode network, the frontoparietal network, the dorsal attention network, and the ventral attention network.[35] In contrast, the prefrontal and parietal cortices of marmosets and other small non-human animals are relatively small, and these networks are not as clearly spatially distinguishable as in humans[51,52] by resting-state functional connectivity, which partly explained the discrepancy between marmosets and humans. However, despite similarities in connectivity patterns between the frontoparietal-like and default-mode-like networks to the cerebellar cortex, their relative connectivity strengths were different. By

(C) The relative size ratio (in percentages) of three nuclei in the three species (top, mouse; middle, marmoset; bottom, macaque).
(D) Mapping the properties of the cerebellar cortex to the nuclei based on their structural connectivity using 80-μm isotropic data. The left shows the cerebellar-lobule labels mapped, and the right is cerebello-cerebral functional gradient 1 mapped on the nuclei. For each panel, the top is coronal slice 325 and the bottom is slice 334. More slices are shown in Figure S5.
(E) Gradient 1 of the functional connectivity between the cerebellar nuclei and the cerebral cortex (nuclei-neocortex gradient 1). For each zoomed-in panel, the top shows nuclei-neocortex gradient 1 of the left nuclei (blue box), and the bottom is the right nuclei (red box).
(F) Functional connectivity (Fisher Z-converted) patterns of two extremes (top 10% and last 10% value of nuclei-neocortex gradient 1) to the left cerebral cortex. The statistical difference was evaluated by paired two-sample t test ($p < 0.05$, false discovery rate [FDR] corrected). The results of the right cerebral cortex are shown in Figure S7. MOTs, motor and premotor cortical regions; DLPFC, dorsolateral prefrontal cortex; MPFC, medial prefrontal cortex; LS, insular cortex; AU, auditory cortex.

using a winner-takes-all approach to map their topological relationship to the cerebellar cortex, we found results similar to those in humans: the frontoparietal-like and default-mode-like network occupied adjacent but distinct zones in non-motor areas of the cerebellar cortex (Figure 5C). Thus, the frontoparietal-like and the default-mode-like networks are spatially distinguishable from the cerebellar mapping of marmosets, consistent with the results in humans.[36,50]

The cerebello-cerebral gradient could not fully explain the intra-cerebral gradient patterns, which suggested that other anatomical features may exist to shape the functional connectivity of the cerebral cortex. As the cerebellar cortex has a remarkably uniform cytoarchitecture and local circuits, which anatomical features may contribute to the gradient patterns of the intra-cerebral connectivity? Recent advances in high-throughput transcriptional sequencing have started to unveil the molecular heterogeneity of the cerebellum.[53,54] By single-cell RNA sequencing of different lobules across the mouse cerebellum, a recent study achieved a comprehensive survey of cell types in the cerebellar cortex and revealed considerable regional specialization in Purkinje neurons and gradient changes in gene expression for cerebellar interneurons.[54] These molecular variations were associated with continuous changes in cell morphologies and electrophysiological properties. By spatially resolved transcriptomics, another study identified regional-specific gene expression patterns with the heterogeneity in Purkinje cells, which had not previously been described in single-cell sequencing studies.[55] The molecular heterogeneity of the cerebellar cortex may be one of the anatomical features that contributes to the gradient patterns of functional connectivity.[56] Future studies integrating both connectivity and gene expression data will be necessary to fully resolve the anatomical basis of the cerebellar functional gradients.

The cerebellar nuclei are key nodes for the cerebello-cerebral circuit loop and receive inputs from the cerebellar cortex and send outputs to other brain regions.[24,37,57] In the mammalian brain, there are three pairs of cerebellar nuclei, with the fastigial nuclei being considered phylogenetically the oldest and the dentate nuclei the youngest.[37,58,59] By brain-wide anterograde neuronal tracing, a previous study revealed distinct projection patterns of the three types of nuclei in mice, with their target regions being shifted relative to each other.[37] Such shifts formed a gradient-changing pattern of connectivity to the cerebellar cortex, where fastigial (medial), interposed, and dentate (lateral) nuclei innervated the vermis (motor), paravermis, and hemisphere (non-motor) of the cerebellar cortex, respectively.

Compared with mice brains, the primate cerebellar nuclei underwent nucleus-specific expansion during evolution (Figure 6C). However, the connectivity of cerebellar nuclei has not been fully explored in the primate brains, for which the neuronal tracing approaches were less accessible. With the high-resolution diffusion MRI and awake resting-state fMRI data, we mapped topological connectivity patterns of the cerebellar nuclei in the cerebello-cerebral circuits of the marmoset brain (Figure 6). The phylogenetically youngest dentate nucleus showed structural connectivity mainly to the Sim and Crus areas of the cerebellar cortex, which are non-motor areas at one extreme of the cerebello-cerebral functional gradient. In contrast, the phylogenetically oldest fastigial nucleus was mostly anatomically connected to lobules I–VI, which are motor areas at the other extreme of the functional gradient. Consistently, the topological pattern was also reflected in the principal gradient of the functional connectivity between the cerebellar nuclei and the neocortex, with the dentate nucleus at one extreme and the fastigial nucleus at the other extreme (Figure 6F). The connectivity patterns of the cerebellar nuclei of the marmoset revealed by diffusion tracking were similar to the patterns seen in the mouse as reported by neurotracing data,[37] indicating the common topological principle of the cerebellar-nuclei connectivity across species. In all, these results provided a comprehensive map of anatomical and functional connectivity patterns of the marmoset cerebellum and characterized the close evolutionary relationship of the cerebello-cerebral circuits.

Limitations of the study

Marmoset Brain Mapping v.5 has provided a comprehensive neuroimaging atlas of the marmoset cerebellum and revealed details of the cerebellar anatomy and connectivity. However, v.5 also faces limitations that may require attention and future modification. First, due to the resolution required to resolve the cerebellar anatomy, we chose to use the *ex vivo* ultra-high-resolution data of one brain sample to build the anatomical atlas rather than the *in vivo* structural MRI data of a population.[12] As the general neuroanatomy of the cerebellum is similar across animals, our atlas can be readily spatially registered to the data of other animals for most applications. However, it would be beneficial to create a population-based atlas based on *ex vivo* ultra-high-resolution data in order to reveal individual variations in the fine-detailed folia patterns. Recently, Brain/MINDS released the largest multi-modal MRI resource of marmoset brains to date,[60] allowing the comprehensive comparison of living and postmortem brains. These new resources will be valuable for understanding the neuroanatomy and connectivity of marmosets and be helpful to resolve the limitations of the current study. Second, based on awake resting-state fMRI, we were able to reconstruct the gradient patterns of the cerebellar functional connectivity. However, the functional domains of the cerebellum, including gross-level non-motor and motor presentations, were not defined and validated by multi-domain task fMRI data.[22] Because of the practice difficulties in instructing animals to perform multi-domain tasks inside MRI scanners, we need other techniques, such as electrophysiology and spatial transcriptome, to explore the functional domains of the marmoset cerebellar cortex. Third, we estimated the connectivity between the cerebellar nuclei and the cerebellar cortex purely by diffusion tractography. Although our ultra-high-resolution data improved the tracking accuracy and the cerebellar white matter is less complex than the cerebral cortex, diffusion tractography has inherent limitations and may not fully replicate real anatomical connections.[61] It is important to examine the real connections underlying the topological relationship between the cerebellar cortex and nuclei by neuronal-tracing data and other cutting-edge techniques.[62–65] Multi-omics integration of different types of data, including our current neuroimaging data, will be an important direction to fully characterize the anatomical and functional architecture of the cerebellum.

STAR★METHODS

Detailed methods are provided in the online version of this paper and include the following:

- KEY RESOURCES TABLE
- RESOURCE AVAILABILITY
  - Lead contact
  - Materials availability
  - Data and code availability
- EXPERIMENTAL MODEL AND SUBJECT DETAILS
  - Marmoset subjects
  - Human subjects
- METHOD DETAILS
  - Lobular parcellations and surface reconstruction
  - Functional connectivity and gradient analysis of the cerebellar cortex
  - Structural-connectivity-based mapping and functional connectivity analysis of the cerebellar nuclei
- QUANTIFICATION AND STATISTICAL ANALYSIS

SUPPLEMENTAL INFORMATION

Supplemental information can be found online at https://doi.org/10.1016/j.celrep.2023.112480.

ACKNOWLEDGMENTS

We thank Dr. Ian Logan for the language editing and commenting on the manuscript. We also thank the 9.4T core facility and Marmoset Animal Facility of the CEBSIT for their assistance in the study. The study was supported by grants from by the National Science and Technology Innovation 2030 Major Program (grant nos. STI2030-2021ZD0203900, 2022ZD0205000, and 2021ZD0200900), the National Natural Science Foundation of China (no. 32171088 to C.L.), the Lingang Laboratory (no. LG-QS-202201-02 to C.L.), and the Shanghai Municipal Science and Technology Major Project (no. 2018SHZDZX05 to C.L.).

AUTHOR CONTRIBUTIONS

C.L. and X.Z. designed the study; X.Z., C.L., Y.Z., and C.W. analyzed the data; X.Z., C.L., and H.Y. constructed the MBM v.5 atlas; F.F., C.L., and X.Z. designed the MBM v.5 online atlas viewer; X.Z. and C.L. wrote the original manuscript; C.L., X.Z., Y.-G.Y., and Y.Z. revised the manuscript; and C.L. and Y.-G.Y. supervised the study.

DECLARATION OF INTERESTS

The authors declare no competing interests.

Received: October 18, 2022
Revised: February 1, 2023
Accepted: April 20, 2023

REFERENCES

1. Okano, H. (2021). Current status of and perspectives on the application of marmosets in neurobiology. Annu. Rev. Neurosci. *44*, 27–48. https://doi.org/10.1146/annurev-neuro-030520-101844.
2. Okano, H., and Mitra, P. (2015). Brain-mapping projects using the common marmoset. Neurosci. Res. *93*, 3–7. https://doi.org/10.1016/j.neures.2014.08.014.
3. Miller, C.T., Freiwald, W.A., Leopold, D.A., Mitchell, J.F., Silva, A.C., and Wang, X. (2016). Marmosets: a neuroscientific model of human social behavior. Neuron *90*, 219–233. https://doi.org/10.1016/j.neuron.2016.03.018.
4. Lin, M.K., Takahashi, Y.S., Huo, B.-X., Hanada, M., Nagashima, J., Hata, J., Tolpygo, A.S., Ram, K., Lee, B.C., Miller, M.I., et al. (2019). A high-throughput neurohistological pipeline for brain-wide mesoscale connectivity mapping of the common marmoset. Elife *8*, e40042. https://doi.org/10.7554/eLife.40042.
5. Schaeffer, D.J., Klassen, L.M., Hori, Y., Tian, X., Szczupak, D., Yen, C.C.-C., Cléry, J.C., Gilbert, K.M., Gati, J.S., Menon, R.S., et al. (2022). An open access resource for functional brain connectivity from fully awake marmosets. Neuroimage *252*, 119030. https://doi.org/10.1016/j.neuroimage.2022.119030.
6. Kita, Y., Nishibe, H., Wang, Y., Hashikawa, T., Kikuchi, S.S., U, M., Yoshida, A.C., Yoshida, C., Kawase, T., Ishii, S., et al. (2021). Cellular-resolution gene expression profiling in the neonatal marmoset brain reveals dynamic species- and region-specific differences. Proc. Natl. Acad. Sci. USA *118*, e2020125118. https://doi.org/10.1073/pnas.2020125118.
7. Woodward, A., Gong, R., Abe, H., Nakae, K., Hata, J., Skibbe, H., Yamaguchi, Y., Ishii, S., Okano, H., Yamamori, T., and Ichinohe, N. (2020). The NanoZoomer artificial intelligence connectomics pipeline for tracer injection studies of the marmoset brain. Brain Struct. Funct. *225*, 1225–1243. https://doi.org/10.1007/s00429-020-02073-y.
8. Woodward, A., Hashikawa, T., Maeda, M., Kaneko, T., Hikishima, K., Iriki, A., Okano, H., and Yamaguchi, Y. (2018). The Brain/MINDS 3D digital marmoset brain atlas. Sci. Data *5*, 180009. https://doi.org/10.1038/sdata.2018.9.
9. Shimogori, T., Abe, A., Go, Y., Hashikawa, T., Kishi, N., Kikuchi, S.S., Kita, Y., Niimi, K., Nishibe, H., Okuno, M., et al. (2018). Digital gene atlas of neonate common marmoset brain. Neurosci. Res. *128*, 1–13. https://doi.org/10.1016/j.neures.2017.10.009.
10. Song, X., Guo, Y., Chen, C., and Wang, X. (2022). A silent two-photon imaging system for studying in vivo auditory neuronal functions. Light Sci. Appl. *11*, 96. https://doi.org/10.1038/s41377-022-00783-y.
11. Gao, L., and Wang, X. (2020). Intracellular neuronal recording in awake nonhuman primates. Nat. Protoc. *15*, 3615–3631. https://doi.org/10.1038/s41596-020-0388-3.
12. Liu, C., Yen, C.C.-C., Szczupak, D., Tian, X., Glen, D., and Silva, A.C. (2021). Marmoset Brain Mapping V3: population multi-modal standard volumetric and surface-based templates. Neuroimage *226*, 117620. https://doi.org/10.1016/j.neuroimage.2020.117620.
13. Liu, C., Ye, F.Q., Newman, J.D., Szczupak, D., Tian, X., Yen, C.C.-C., Majka, P., Glen, D., Rosa, M.G.P., Leopold, D.A., and Silva, A.C. (2020). A resource for the detailed 3D mapping of white matter pathways in the marmoset brain. Nat. Neurosci. *23*, 271–280. https://doi.org/10.1038/s41593-019-0575-0.
14. Liu, C., Ye, F.Q., Yen, C.C.-C., Newman, J.D., Glen, D., Leopold, D.A., and Silva, A.C. (2018). A digital 3D atlas of the marmoset brain based on multi-modal MRI. Neuroimage *169*, 106–116. https://doi.org/10.1016/j.neuroimage.2017.12.004.
15. Tian, X., Chen, Y., Majka, P., Szczupak, D., Perl, Y.S., Yen, C.C.-C., Tong, C., Feng, F., Jiang, H., Glen, D., et al. (2020). An integrated resource for functional and structural connectivity of the marmoset brain. Nat. Commun. *13*, 7416. https://doi.org/10.1038/s41467-022-35197-2.
16. Majka, P., Bai, S., Bakola, S., Bednarek, S., Chan, J.M., Jermakow, N., Passarelli, L., Reser, D.H., Theodoni, P., Worthy, K.H., et al. (2020). Open access resource for cellular-resolution analyses of corticocortical connectivity in the marmoset monkey. Nat. Commun. *11*, 1133. https://doi.org/10.1038/s41467-020-14858-0.
17. Majka, P., Chaplin, T.A., Yu, H.-H., Tolpygo, A., Mitra, P.P., Wójcik, D.K., and Rosa, M.G.P. (2016). Towards a comprehensive atlas of cortical connections in a primate brain: mapping tracer injection studies of the

common marmoset into a reference digital template. J. Comp. Neurol. *524*, 2161–2181. https://doi.org/10.1002/cne.24023.

18. Theodoni, P., Majka, P., Reser, D.H., Wójcik, D.K., Rosa, M.G.P., and Wang, X.-J. (2021). Structural attributes and principles of the neocortical connectome in the marmoset monkey. Cerebr. Cortex *32*, 15–28. https://doi.org/10.1093/cercor/bhab191.
19. Paxinos, G., Watson, C., Petrides, M., Rosa, M., and Tokuno, H. (2012). The Marmoset Brain in Stereotaxic Coordinates (Elsevier Academic Press).
20. Hardman, C.D., and Ashwell, K.W.S. (2012). Stereotaxic and Chemoarchitectural Atlas of the Brain of the Common Marmoset (Callithrix jacchus) (CRC Press).
21. Buckner, R.L. (2013). The cerebellum and cognitive function: 25 years of insight from anatomy and neuroimaging. Neuron *80*, 807–815. https://doi.org/10.1016/j.neuron.2013.10.044.
22. King, M., Hernandez-Castillo, C.R., Poldrack, R.A., Ivry, R.B., and Diedrichsen, J. (2019). Functional boundaries in the human cerebellum revealed by a multi-domain task battery. Nat. Neurosci. *22*, 1371–1378. https://doi.org/10.1038/s41593-019-0436-x.
23. Strick, P.L., Dum, R.P., and Fiez, J.A. (2009). Cerebellum and nonmotor function. Annu. Rev. Neurosci. *32*, 413–434. https://doi.org/10.1146/annurev.neuro.31.060407.125606.
24. Wagner, M.J., and Luo, L. (2020). Neocortex–cerebellum circuits for cognitive processing. Trends Neurosci. *43*, 42–54. https://doi.org/10.1016/j.tins.2019.11.002.
25. Guell, X., Schmahmann, J.D., Gabrieli, J.D., and Ghosh, S.S. (2018). Functional gradients of the cerebellum. Elife *7*, e36652. https://doi.org/10.7554/eLife.36652.
26. Guell, X. (2022). Functional gradients of the cerebellum: a review of practical applications. Cerebellum *21*, 1061–1072. https://doi.org/10.1007/s12311-021-01342-8.
27. Liu, X., d'Oleire Uquillas, F., Viaene, A.N., Zhen, Z., and Gomez, J. (2022). A multifaceted gradient in human cerebellum of structural and functional development. Nat. Neurosci. *25*, 1129–1133. https://doi.org/10.1038/s41593-022-01136-z.
28. De Zeeuw, C.I., Lisberger, S.G., and Raymond, J.L. (2021). Diversity and dynamism in the cerebellum. Nat. Neurosci. *24*, 160–167. https://doi.org/10.1038/s41593-020-00754-9.
29. Diedrichsen, J., King, M., Hernandez-Castillo, C., Sereno, M., and Ivry, R.B. (2019). Universal transform or multiple functionality? Understanding the contribution of the human cerebellum across task domains. Neuron *102*, 918–928. https://doi.org/10.1016/j.neuron.2019.04.021.
30. Fischl, B. (2012). FreeSurfer. Neuroimage *62*, 774–781. https://doi.org/10.1016/j.neuroimage.2012.01.021.
31. Diedrichsen, J., and Zotow, E. (2015). Surface-based display of volume-averaged cerebellar imaging data. PLoS One *10*, e0133402. https://doi.org/10.1371/journal.pone.0133402.
32. Sereno, M.I., Diedrichsen, J., Tachrount, M., Testa-Silva, G., d'Arceuil, H., and De Zeeuw, C. (2020). The human cerebellum has almost 80% of the surface area of the neocortex. Proc. Natl. Acad. Sci. USA *117*, 19538–19543. https://doi.org/10.1073/pnas.2002896117.
33. Margulies, D.S., Ghosh, S.S., Goulas, A., Falkiewicz, M., Huntenburg, J.M., Langs, G., Bezgin, G., Eickhoff, S.B., Castellanos, F.X., Petrides, M., et al. (2016). Situating the default-mode network along a principal gradient of macroscale cortical organization. Proc. Natl. Acad. Sci. USA *113*, 12574–12579. https://doi.org/10.1073/pnas.1608282113.
34. Vos de Wael, R., Benkarim, O., Paquola, C., Lariviere, S., Royer, J., Tavakol, S., Xu, T., Hong, S.-J., Langs, G., Valk, S., et al. (2020). BrainSpace: a toolbox for the analysis of macroscale gradients in neuroimaging and connectomics datasets. Commun. Biol. *3*, 103. https://doi.org/10.1038/s42003-020-0794-7.
35. Yeo, B.T.T., Krienen, F.M., Sepulcre, J., Sabuncu, M.R., Lashkari, D., Hollinshead, M., Roffman, J.L., Smoller, J.W., Zöllei, L., Polimeni, J.R., et al. (2011). The organization of the human cerebral cortex estimated by intrinsic functional connectivity. J. Neurophysiol. *106*, 1125–1165. https://doi.org/10.1152/jn.00338.2011.
36. Buckner, R.L., Krienen, F.M., Castellanos, A., Diaz, J.C., and Yeo, B.T.T. (2011). The organization of the human cerebellum estimated by intrinsic functional connectivity. J. Neurophysiol. *106*, 2322–2345. https://doi.org/10.1152/jn.00339.2011.
37. Kebschull, J.M., Richman, E.B., Ringach, N., Friedmann, D., Albarran, E., Kolluru, S.S., Jones, R.C., Allen, W.E., Wang, Y., Cho, S.W., et al. (2020). Cerebellar nuclei evolved by repeatedly duplicating a conserved cell-type set. Science *370*, eabd5059. https://doi.org/10.1126/science.abd5059.
38. Balsters, J.H., Cussans, E., Diedrichsen, J., Phillips, K.A., Preuss, T.M., Rilling, J.K., and Ramnani, N. (2010). Evolution of the cerebellar cortex: the selective expansion of prefrontal-projecting cerebellar lobules. Neuroimage *49*, 2045–2052. https://doi.org/10.1016/j.neuroimage.2009.10.045.
39. Barton, R.A., and Harvey, P.H. (2000). Mosaic evolution of brain structure in mammals. Nature *405*, 1055–1058. https://doi.org/10.1038/35016580.
40. Barton, R.A., and Venditti, C. (2014). Rapid evolution of the cerebellum in humans and other great apes. Curr. Biol. *24*, 2440–2444. https://doi.org/10.1016/j.cub.2014.08.056.
41. Thiebaut de Schotten, M., Croxson, P.L., and Mars, R.B. (2019). Large-scale comparative neuroimaging: where are we and what do we need? Cortex *118*, 188–202. https://doi.org/10.1016/j.cortex.2018.11.028.
42. Friedrich, P., Forkel, S.J., Amiez, C., Balsters, J.H., Coulon, O., Fan, L., Goulas, A., Hadj-Bouziane, F., Hecht, E.E., Heuer, K., et al. (2021). Imaging evolution of the primate brain: the next frontier? Neuroimage *228*, 117685. https://doi.org/10.1016/j.neuroimage.2020.117685.
43. Tendler, B.C., Hanayik, T., Ansorge, O., Bangerter-Christensen, S., Berns, G.S., Bertelsen, M.F., Bryant, K.L., Foxley, S., van den Heuvel, M.P., Howard, A.F.D., et al. (2022). The Digital Brain Bank, an open access platform for post-mortem imaging datasets. Elife *11*, e73153. https://doi.org/10.7554/eLife.73153.
44. Mars, R.B., Jbabdi, S., and Rushworth, M.F.S. (2021). A common space approach to comparative neuroscience. Annu. Rev. Neurosci. *44*, 69–86. https://doi.org/10.1146/annurev-neuro-100220-025942.
45. Burt, J.B., Demirtaş, M., Eckner, W.J., Navejar, N.M., Ji, J.L., Martin, W.J., Bernacchia, A., Anticevic, A., and Murray, J.D. (2018). Hierarchy of transcriptomic specialization across human cortex captured by structural neuroimaging topography. Nat. Neurosci. *21*, 1251–1259. https://doi.org/10.1038/s41593-018-0195-0.
46. Vogel, J.W., Alexander-Bloch, A., Wagstyl, K., Bertolero, M., Markello, R., Pines, A., Sydnor, V.J., Diaz-Papkovich, A., Hansen, J., Evans, A.C., et al. (2022). Conserved Whole-Brain Spatiomolecular Gradients Shape Adult Brain Functional Organization. https://doi.org/10.1101/2022.09.18.508425.
47. Vázquez-Rodríguez, B., Suárez, L.E., Markello, R.D., Shafiei, G., Paquola, C., Hagmann, P., van den Heuvel, M.P., Bernhardt, B.C., Spreng, R.N., and Misic, B. (2019). Gradients of structure–function tethering across neocortex. Proc. Natl. Acad. Sci. USA *116*, 21219–21227. https://doi.org/10.1073/pnas.1903403116.
48. Atapour, N., Majka, P., Wolkowicz, I.H., Malamanova, D., Worthy, K.H., and Rosa, M.G.P. (2019). Neuronal distribution across the cerebral cortex of the marmoset monkey (*Callithrix jacchus*). Cerebr. Cortex *29*, 3836–3863, 1991. https://doi.org/10.1093/cercor/bhy263.
49. Tong, C., Liu, C., Zhang, K., Bo, B., Xia, Y., Yang, H., Feng, Y., and Liang, Z. (2022). Multimodal analysis demonstrating the shaping of functional gradients in the marmoset brain. Nat. Commun. *13*, 6584. https://doi.org/10.1038/s41467-022-34371-w.
50. Ji, J.L., Spronk, M., Kulkarni, K., Repovš, G., Anticevic, A., and Cole, M.W. (2019). Mapping the human brain's cortical-subcortical functional network organization. Neuroimage *185*, 35–57. https://doi.org/10.1016/j.neuroimage.2018.10.006.
51. Garin, C.M., Hori, Y., Everling, S., Whitlow, C.T., Calabro, F.J., Luna, B., Froesel, M., Gacoin, M., Ben Hamed, S., Dhenain, M., and Constantinidis,

C. (2022). An evolutionary gap in primate default mode network organization. Cell Rep. *39*, 110669. https://doi.org/10.1016/j.celrep.2022.110669.

52. Liu, C., Yen, C.C.-C., Szczupak, D., Ye, F.Q., Leopold, D.A., and Silva, A.C. (2019). Anatomical and functional investigation of the marmoset default mode network. Nat. Commun. *10*, 1975. https://doi.org/10.1038/s41467-019-09813-7.
53. Chen, X., Du, Y., Broussard, G.J., Kislin, M., Yuede, C.M., Zhang, S., Dietmann, S., Gabel, H., Zhao, G., Wang, S.S.-H., et al. (2022). Transcriptomic mapping uncovers Purkinje neuron plasticity driving learning. Nature *605*, 722–727. https://doi.org/10.1038/s41586-022-04711-3.
54. Kozareva, V., Martin, C., Osorno, T., Rudolph, S., Guo, C., Vanderburg, C., Nadaf, N., Regev, A., Regehr, W.G., and Macosko, E. (2021). A transcriptomic atlas of mouse cerebellar cortex comprehensively defines cell types. Nature *598*, 214–219. https://doi.org/10.1038/s41586-021-03220-z.
55. Rodriques, S.G., Stickels, R.R., Goeva, A., Martin, C.A., Murray, E., Vanderburg, C.R., Welch, J., Chen, L.M., Chen, F., and Macosko, E.Z. (2019). Slide-seq: a scalable technology for measuring genome-wide expression at high spatial resolution. Science *363*, 1463–1467. https://doi.org/10.1126/science.aaw1219.
56. Wang, Y., Chai, L., Chu, C., Li, D., Gao, C., Wu, X., Yang, Z., Zhang, Y., Xu, J., Nyengaard, J.R., et al. (2022). Uncovering the genetic profiles underlying the intrinsic organization of the human cerebellum. Mol. Psychiatr. *27*, 2619–2634. https://doi.org/10.1038/s41380-022-01489-8.
57. Gao, Z., Davis, C., Thomas, A.M., Economo, M.N., Abrego, A.M., Svoboda, K., De Zeeuw, C.I., and Li, N. (2018). A cortico-cerebellar loop for motor planning. Nature *563*, 113–116. https://doi.org/10.1038/s41586-018-0633-x.
58. Diedrichsen, J., Maderwald, S., Küper, M., Thürling, M., Rabe, K., Gizewski, E.R., Ladd, M.E., and Timmann, D. (2011). Imaging the deep cerebellar nuclei: a probabilistic atlas and normalization procedure. Neuroimage *54*, 1786–1794. https://doi.org/10.1016/j.neuroimage.2010.10.035.
59. Dimitrova, A., Zeljko, D., Schwarze, F., Maschke, M., Gerwig, M., Frings, M., Beck, A., Aurich, V., Forsting, M., and Timmann, D. (2006). Probabilistic 3D MRI atlas of the human cerebellar dentate/interposed nuclei. Neuroimage *30*, 12–25. https://doi.org/10.1016/j.neuroimage.2005.09.020.
60. Hata, J., Nakae, K., Tsukada, H., Woodward, A., Haga, Y., Iida, M., Uematsu, A., Seki, F., Ichinohe, N., Gong, R., et al. (2023). Multi-modal Brain Magnetic Resonance Imaging Database Covering Marmosets with a Wide Age Range. Sci. Data *10*, 221. https://doi.org/10.1038/s41597-023-02121-2.
61. Thomas, C., Ye, F.Q., Irfanoglu, M.O., Modi, P., Saleem, K.S., Leopold, D.A., and Pierpaoli, C. (2014). Anatomical accuracy of brain connections derived from diffusion MRI tractography is inherently limited. Proc. Natl. Acad. Sci. USA *111*, 16574–16579. https://doi.org/10.1073/pnas.1405672111.
62. Shen, Y., Ding, L.-F., Yang, C.-Y., Xu, F., Lau, P.-M., and Bi, G.-Q. (2022). Mapping big brains at subcellular resolution in the era of big data in zoology. Zool. Res. *43*, 597–599. https://doi.org/10.24272/j.issn.2095-8137.2022.138.
63. Gao, L., Liu, S., Gou, L., Hu, Y., Liu, Y., Deng, L., Ma, D., Wang, H., Yang, Q., Chen, Z., et al. (2022). Single-neuron projectome of mouse prefrontal cortex. Nat. Neurosci. *25*, 515–529. https://doi.org/10.1038/s41593-022-01041-5.
64. Qu, L., Li, Y., Xie, P., Liu, L., Wang, Y., Wu, J., Liu, Y., Wang, T., Li, L., Guo, K., et al. (2022). Cross-modal coherent registration of whole mouse brains. Nat. Methods *19*, 111–118. https://doi.org/10.1038/s41592-021-01334-w.
65. Xu, F., Shen, Y., Ding, L., Yang, C.-Y., Tan, H., Wang, H., Zhu, Q., Xu, R., Wu, F., Xiao, Y., et al. (2021). High-throughput mapping of a whole rhesus monkey brain at micrometer resolution. Nat. Biotechnol. *39*, 1521–1528. https://doi.org/10.1038/s41587-021-00986-5.
66. Zuo, X.-N., Anderson, J.S., Bellec, P., Birn, R.M., Biswal, B.B., Blautzik, J., Breitner, J.C.S., Buckner, R.L., Calhoun, V.D., Castellanos, F.X., et al. (2014). An open science resource for establishing reliability and reproducibility in functional connectomics. Sci. Data *1*, 140049. https://doi.org/10.1038/sdata.2014.49.
67. Yushkevich, P.A., Piven, J., Hazlett, H.C., Smith, R.G., Ho, S., Gee, J.C., and Gerig, G. (2006). User-guided 3D active contour segmentation of anatomical structures: significantly improved efficiency and reliability. Neuroimage *31*, 1116–1128. https://doi.org/10.1016/j.neuroimage.2006.01.015.
68. Marcus, D.S., Harwell, J., Olsen, T., Hodge, M., Glasser, M.F., Prior, F., Jenkinson, M., Laumann, T., Curtiss, S.W., and Van Essen, D.C. (2011). Informatics and data mining tools and strategies for the human connectome project. Front. Neuroinform. *5*, 4. https://doi.org/10.3389/fninf.2011.00004.
69. Cox, R.W. (2012). AFNI: what a long strange trip it's been. Neuroimage *62*, 743–747. https://doi.org/10.1016/j.neuroimage.2011.08.056.
70. Tournier, J.-D., Smith, R., Raffelt, D., Tabbara, R., Dhollander, T., Pietsch, M., Christiaens, D., Jeurissen, B., Yeh, C.-H., and Connelly, A. (2019). MRtrix3: a fast, flexible and open software framework for medical image processing and visualisation. Neuroimage *202*, 116137. https://doi.org/10.1016/j.neuroimage.2019.116137.
71. Diedrichsen, J., Balsters, J.H., Flavell, J., Cussans, E., and Ramnani, N. (2009). A probabilistic MR atlas of the human cerebellum. Neuroimage *46*, 39–46. https://doi.org/10.1016/j.neuroimage.2009.01.045.
72. Boillat, Y., Bazin, P.-L., O'Brien, K., Fartaria, M.J., Bonnier, G., Krueger, G., van der Zwaag, W., and Granziera, C. (2018). Surface-based characteristics of the cerebellar cortex visualized with ultra-high field MRI. Neuroimage *172*, 1–8. https://doi.org/10.1016/j.neuroimage.2018.01.016.
73. Van Essen, D.C. (2002). Surface-based atlases of cerebellar cortex in the human, macaque, and mouse. Ann. N. Y. Acad. Sci. *978*, 468–479. https://doi.org/10.1111/j.1749-6632.2002.tb07588.x.
74. Ullmann, J.F.P., Watson, C., Janke, A.L., Kurniawan, N.D., and Reutens, D.C. (2013). A segmentation protocol and MRI atlas of the C57BL/6J mouse neocortex. Neuroimage *78*, 196–203. https://doi.org/10.1016/j.neuroimage.2013.04.008.

STAR★METHODS

KEY RESOURCES TABLE

REAGENT or RESOURCE	SOURCE	IDENTIFIER
Deposited data		
Marmoset Brain Mapping project	(Liu et al.)[12]	https://marmosetbrainmapping.org/
The Hangzhou Normal University of the Consortium for Reliability and Reproducibility	(Zuo et al.)[66]	http://fcon_1000.projects.nitrc.org/indi/CoRR/html/hnu_1.html
Software and algorithms		
MATLAB version 2020a	MathWorks	https://www.mathworks.com
ITK-SNAP Version 3.8.0	(Yushkevich et al.)[67]	http://www.itksnap.org/pmwiki/pmwiki.php
Connectome Workbench Version 1.4.2	(Marcus et al.)[68]	https://www.humanconnectome.org/software/connectome-workbench
AFNI Version 22.1.10	(Cox et al.)[69]	https://afni.nimh.nih.gov/
Freesurfer Version 3.0	(Fischl et al.)[30]	https://surfer.nmr.mgh.harvard.edu/
Mrtrix 3.0.1	(Tournier et al.)[70]	https://www.mrtrix.org/
Other		
Human cerebral networks atlas	(Yeo et al.)[35]	https://pubmed.ncbi.nlm.nih.gov/21653723/
Human cerebellar cortex flat map.	(Diedrichsen et al.)[31]	https://pubmed.ncbi.nlm.nih.gov/26230510/
Original code	This paper	Zenoda Data: https://doi.org/10.5281/zenodo.7807792

RESOURCE AVAILABILITY

Lead contact

Further information and requests for resources and reagents should be directed to and will be fulfilled by the lead contact, CIRONG LIU (crliu@ion.ac.cn).

Materials availability

This study did not generate new unique reagents.

Data and code availability

- This paper analyzes existing and publicly available data. The accession number of the dataset is listed in the key resources table. The atlases have been deposited at marmosetbrainmapping.org/MBMv5.html.
- All original code has been deposited at Zenodo and is publicly available. DOIs are listed in the key resources table.
- Any additional information required to reanalyze the data reported in this paper is available from the lead contact upon request.

EXPERIMENTAL MODEL AND SUBJECT DETAILS

Marmoset subjects

All marmoset data used in this study were collected from the *Marmoset Brain Mapping* project (*marmosetbrainmapping.org*), and all procedures were approved by the Animal Care and Use Committee (ACUC) of the Institute of Neuroscience, Chinese Academy of Sciences. The ultra-high resolution multi-modal *ex-vivo* data, from version 2 (MBMv2) of the *Marmoset Brain Mapping* project,[13] were used to create the lobular parcellation, reconstruct fine-grained surfaces, and estimate structural connectivity. The *ex-vivo* data were collected on a 7T/30cm MRI (Bruker Biospin) with a 30-mm ID quadrature millipede coil (ExtendMR, LLC, Milpitas, CA), including 80 μm and 64 μm isotropic multi-shell diffusion MRI (dMRI), 80 μm isotropic MTR, and 50 μm isotropic T2*-weighted and T2-weighted images. The multi-shell dMRI had three b values and 204 DWI directions (8 b = 0, 6 b = 30, 64 b = 2400, and 126 b = 4800). The 64 μm isotropic data were collected from a male marmoset of 10.9-year-old, and all the other data were from a male of 4.5-year-old. Detailed scanning protocol was described in the MBMv2 resource paper.[13] The awake resting-state fMRI data, from version 4 (MBMv4) of the *Marmoset Brain Mapping* project[15] were used to examine the functional connectivity and gradient patterns of the cerebellum. The data was collected from 39 marmosets (31 males and 8 females, mean age = 4-year

old), which were scanned repeatedly and resulted in a total of 710 fMRI runs (17 min per run). All resting-state fMRI data had a temporal resolution of TR = 2s, and a spatial resolution of 0.5 mm isotropic and were scanned using two opposite phase-encoding directions (left-to-right and right-to-left) to compensate for Echo Planar Imaging (EPI) distortions and signal dropouts. Besides, for each session, a T2-weighted image was scanned for spatial registration. A detailed scanning protocol and animal information of the resting-state fMRI can be found in the MBMv4 resource paper.[15]

Human subjects

Human data were from "The Hangzhou Normal University of the Consortium for Reliability and Reproducibility (CoRR-HNU) dataset",[66] consisting of 30 young healthy adults (15 females, mean age = 24). The detailed information of the data can be found at http://fcon_1000.projects.nitrc.org/indi/CoRR/html/hnu_1.html.

METHOD DETAILS

Lobular parcellations and surface reconstruction

To create a fine-detailed surface of the marmoset cerebellar cortex, the cerebellum was extracted from the 80 μm multi-modal templates of the MBMv2. The ultra-high resolution and multi-modalities of the MBMv2 provided rich contrasts to visually distinguish the fine-detailed folia patterns of the cerebellar cortex. According to the anatomical annotation of the Paxinos atlas[19] and folia patterns, the cerebellum was manually segmented into the gray matter and the white matter tissue types and parcellated into different lobules using ITK-Snap.[67] The digital delineated lobules included I, II, III, IV, V, VI, VII, VIII, IX, X, SIM, Par, Cop, Fl, PFl, Crus I and Crus II, a total of 17 lobules. The I, II, III, and IV were merged into one region (I-IV), and the IX and X were merged into one (IX-X) to form a 13-lobule parcellation, similar to previous studies for the human cerebellar atlas.[31,71] These lobule parcellations and tissue-type segmentation constituted the volumetric atlas of the marmoset cerebellar cortex.

Surfaces and flat maps were shown to be useful tools to visualize and analyze cerebellar imaging data.[31,32,72,73] Based on the volumetric atlas, fine-detailed surfaces of the cerebellar cortex were generated using the Freesurfer.[30] As tailored for *in-vivo* structural images of human brains, the Freesurfer would not work appropriately on our high-resolution *ex-vivo* images of the marmoset cerebellum. Therefore, related images were modified to conform to the requirements of the Freesurfer. First, the T2*-image, the gray matter, and the white matter segmentation maps of the cerebellum were resampled to an RSP orientation (Right-to-left, Superior-to-inferior, and Posterior-to-anterior), and the resolution information in image headers was modified from 80 μm × 80 μm x 80 μm–100 μm × 100 μm x 100 μm (note that only the header was modified, the images themselves were not downsampled). The value of the white matter segment was set to 127 or 255 for the surface tessellation (equivalent to the *mri_fill*) to create an original white matter surface of the cerebellum. Then, the gray matter and the white matter segments were merged, assigned specific values for each tissue type, and smoothed into a combined image. The pial surface of the cerebellar cortex was generated from the original white matter surface by the *mris_make_surfaces* command with modified parameters. The paired two surfaces were smoothed and manually adjusted to remove errors during surface generation. To create the flat map of the cerebellar cortex, the white matter surfaces were inflated by the *mris_inflate*, and sphere surfaces were created by the *mris_sphere*. Volumetric lobular parcellations were mapped to these surfaces by the ribbon method of the *wb_command* of the Connectome Workbench.[68] Guided by the curvature map and the lobular parcellations, the inflated surface was manually cut and flattened by the *mris_flatten*. The raw flat map was then manually optimized using an in-house method to improve the visualization. Together, the white matter surface, pial surface, flat map, associated curvature map, and lobular-parcellation surface map, constituted the surface-based tool of our atlas.

Our atlas was generated from *ex-vivo* MRI data of brain samples, and the brain sample may expand or shrink during the fixation, preparation, and storage. When using the *ex-vivo* data to estimate the volume of the cerebellum, the expansion or shrinkage of the volume should be corrected. Thus, we calculated the total volumes of the cerebellum using the *ex-vivo* data of the MBMv2 template[13] and the population *in-vivo* templates of the MBMv3,[12] respectively. The volume ratio between the *ex-vivo* data and *in-vivo* data was then used to correct the expansion or shrinkage effect when estimating the volume of the cerebellar lobules.

All surfaces and flat maps were released in the standard GIFTI format, which is compatible with commonly-used surface-based visualization and analyzing tools, including Connectome Workbench, AFNI/SUMA,[69] and Freesurfer.[30] The lobular parcellation was also mapped onto the high-resolution surfaces of the cerebellar cortex and released in NIFTI format and GIFTI format.

Functional connectivity and gradient analysis of the cerebellar cortex

Based on our recently published resting-state fMRI resource (MBMv4) of the marmoset,[15] we analyzed the functional connectivity patterns of the marmoset cerebellum. The preprocessed data "regrBMWC0" of the MBMv4 were used in the following analysis, which represented data with band-passing and temporal denoising of motion parameters, motion-censors, white matter signals, and cerebrospinal fluid (CSF) signals. The above nuisance signal regression (motions, white matter signals, and CSF signals) and bandpassing filtering were conducted in a single regression model by the "3dDeconvolve" and "3dTproject" commands of AFNI. The preprocess of the human data was similar as the marmoset, including slice timing correction, motion correction, spatial normalization into MNI space, resampling to 3 × 3 × 3 mm voxels and smoothing with a Gaussian kernel (FWHM = 6 mm). Friston-24 parameters of head motion, white matter and ventricle signals were regressed out, followed by linear drift correction and temporal filtering (0.01–0.1 Hz).

The diffusion map embedding was used to estimate the functional-gradient patterns of the cerebellum.[33,34] Similar to a previous study on gradients of the human cerebellum,[25] we analyzed the functional gradients on two types of connectivity: 1) the intra-cerebellar functional connectivity that included only the vertices of the cerebellar cortex, emphasizing the intrinsic organization of the cerebellar cortex; and 2) the functional connectivity between the cerebellar cortex and the cerebral cortex, emphasizing the cerebello-cerebral communications.

To obtain the functional gradients, the preprocessed cerebellar data were first mapped to the surface of the cerebral cortex and smoothed with a 1mm FWHM kernel on the surface. To improve computational efficiency, 5000 regions of Interest (ROIs) were generated on the cerebellar inflated surface based on their spatial information (10000 and 20000 ROIs were also evaluated and the resulting functional gradients were similar to the 5000 ROIs). The Pearson correlation between each pair of cerebellar ROIs was calculated to form the matrix of the intra-cerebellar functional connectivity. The correlation between cerebellar ROIs and voxels of the cerebral cortex was calculated to form the matrix of cerebello-cerebral functional connectivity. The diffusion map embedding method was applied to these matrices by the BrainSpace,[34] which nonlinearly dimensionality reduced the matrices into several orthogonalized gradients accounting for as much data variance as possible. The gradient analysis was performed on population-averaged correlation matrices and on the correlation matrices of each marmoset to examine the individual variabilities for each gradient. Take the principal gradient (gradient-1) for example, we calculated the mean and standard deviation (variance) value from the gradient-1 maps of all marmosets and then divided the variance by the mean to obtain a map that reflected the individual variabilities of the gradients.

To examine cerebellar functional connectivity to the 15 functional networks of the marmoset cerebral cortex from awake resting-state fMRI,[15] we calculated the Pearson correlation between the time series of each cerebellar vertices and the mean time series of each contralateral network, which generated a 286308 (vertices) x 15 (networks) matrix. For each vertex, we calculated the mean and variance of the correlations to the fifteen networks and then divided the variance by the mean to obtain a map of the coefficient of variation. The map reflected the specificity of the functional connectivity between these networks and the cerebellar cortex.

Structural-connectivity-based mapping and functional connectivity analysis of the cerebellar nuclei

The cerebellar nuclei were manually delineated on the MRI templates of the MBMv2 (80-μm isotropic resolution),[10] including the dentate nucleus, interposed nucleus, and fastigial nucleus, using the ITK-Snap.[67] For cross-species comparisons, the three nuclei were also delineated on previously published *ex-vivo* MRI templates of C57BL/6 mice (30 μm isotropic resolution)[74] and *ex-vivo* MRI data of rhesus macaque (250 μm isotropic resolution).[13]

To map the topological relationship of the connectivity between cerebellar nuclei and the cerebellar cortex, diffusion tractography was used to estimate their structural connectivity based on ultra-high resolution dMRI data. The main results reported were based on the 80 μm dMRI data of the MBMv2 resource.[10] To verify the results, we also performed a similar analysis on the 150 μm high-b-value dMRI data of the MBMv1.[14] The detailed data collection and preprocessing protocols were described in our previous paper.[66]

The software Mrtrix3 was used for all diffusion tracking.[70] Following its standard pipeline, the *dwi2response* was used to estimate the response function of the preprocessed dMRI data by the *dhollander* method. The *dwi2fod* was used to calculate the fiber orientation distributions (FOD) images by the spherical deconvolution of the multi-shell multi-tissue CSD algorithm. The FOD images were then used for diffusion tracking by the iFOD2 algorithm implemented in the *tckgen* command. Each voxel of nuclei was used as the seed and the tracking was performed within the cerebellum by the *tckgen* to obtain the tracking probability map of each nucleus voxel. For each probability map, the percentages of the selected streamlines that reached different cerebellar lobules were calculated. A winner-takes-all strategy was then applied to the maps, which assigned each nucleus voxel with the voxel of the cerebral cortex that had the largest tracking probability. As such, a topological map between the cerebellar cortex and the cerebellar nuclei was built by structural connectivity. Based on the topological correspondence, the lobule parcellation and functional gradients of the cerebellar cortex were projected to the cerebellar nuclei. To reveal the functional relationship between the cerebellar nuclei and the cerebral cortex, we calculated the functional gradient patterns of the two regions with the same method described previously.[25] In brief, the fMRI data of the nuclei were smoothed with a 0.1 mm FWHM kernel (because of the small size of the nuclei, we used a small smooth kernel). The functional connectivity between each nucleus voxel and the voxels of the cerebral cortex was calculated. The diffusion map embedding method was then applied to the correlation matrices to obtain the functional gradients of the connectivity between the cerebellar nuclei and the cerebral cortex. We then examined the functional connectivity maps of the positive and the negative extremes of the principal gradient. The mean time series of the top 10% voxels of the two extremes were extracted respectively and their correlations to the cerebral cortex were calculated and converted with the Fisher Z-transformation. A paired two-sample t test was used to compare the functional connectivity maps of the two extremes, and the multiple comparisons were corrected by the false discovery rate (FDR, adjusted p value <0.05).

QUANTIFICATION AND STATISTICAL ANALYSIS

All subsequent analyses and visualizations were performed in MATLAB version 2020a (MathWorks), ITK-SNAP Version 3.8.0, Connectome Workbench Version 1.4.2, AFNI Version 22.1.10, and Freesurfer Version 3.0, Mrtrix 3.0.1.

Cell Reports, Volume *42*

Supplemental information

An anatomical and connectivity atlas of the marmoset cerebellum

Xiaojia Zhu, Haotian Yan, Yafeng Zhan, Furui Feng, Chuanyao Wei, Yong-Gang Yao, and Cirong Liu

An Anatomical and Connectivity Atlas of the Marmoset Cerebellum

Xiaojia Zhu[1,2,3], Haotian Yan[2], Yafeng Zhan[2], Furui Feng[2], Chuanyao Wei[2,3], Yong-Gang Yao[1,3,*], Cirong Liu[2,3,*]

[1] Key Laboratory of Animal Models and Human Disease Mechanisms, of the Chinese Academy of Sciences and Yunnan Province, and KIZ-CUHK Joint Laboratory of Bioresources and Molecular Research in Common Diseases, National Research Facility for Phenotypic & Genetic Analysis of Model Animals (Primate Facility), National Resource Center for Non-Human Primates, Kunming Institute of Zoology, Chinese Academy of Sciences, Kunming, 650201, China

[2] Center for Excellence in Brain Science and Intelligence Technology, Institute of Neuroscience, Chinese Academy of Sciences, Shanghai, 200031, China

[3] University of Chinese Academy of Sciences, Beijing, 100049, China

* Co-corresponding authors

Dr. Cirong Liu, E-mail: crliu@ion.ac.cn or Dr. Yong-Gang Yao, E-mail: yaoyg@mail.kiz.ac.cn

Supplementary Tables and Figures

Table S1. The surface areas (mm^2) of 17 lobules estimated from data with different spatial resolutions. The 17 lobules include Lingula I (I), Central lobule II (II), Culmen III (III), Declive IV (IV), lobule V (V), Folium VI (VI), Tuber VII (VII), Pyramid VIII (VIII), Uvula IX (IX), Nodulus X (X), Simplex lobule (SIM), Paramedian lobule (Par), Copula (Cop), Flocculus (Fl), Paraflocculus (PFl), Crus I and Crus II.

Lobules	**I**	**II**	**III**	**IV**	**V**	**VI**	**VII**	**VIII**	**IX**
80 μm	8.05	51.50	79.09	80.88	181.26	100.73	79.99	108.59	90.94
150 μm	1.79	34.48	58.41	66.14	154.23	92.39	65.35	89.96	72.03
250 μm	1.49	27.69	47.54	53.13	123.30	78.57	50.55	75.41	55.55
500 μm	1.14	22.60	30.79	33.17	82.36	39.54	41.32	51.21	39.38
Lobules	**X**	**SIM**	**Par**	**Cop**	**Fl**	**PFl**	**Crus I**	**Crus II**	
80 μm	52.59	221.35	118.06	156.76.8	10.97	260.87	52.92	128.27	
150 μm	34.71	5.44	104.20	96.73	164.98	49.32	99.23	193.57	
250 μm	28.24	5.18	80.76	84.99	123.01	36.89	83.52	168.40	
500 μm	15.97	5.15	47.05	50.15	77.36	38.34	50.32	104.53	

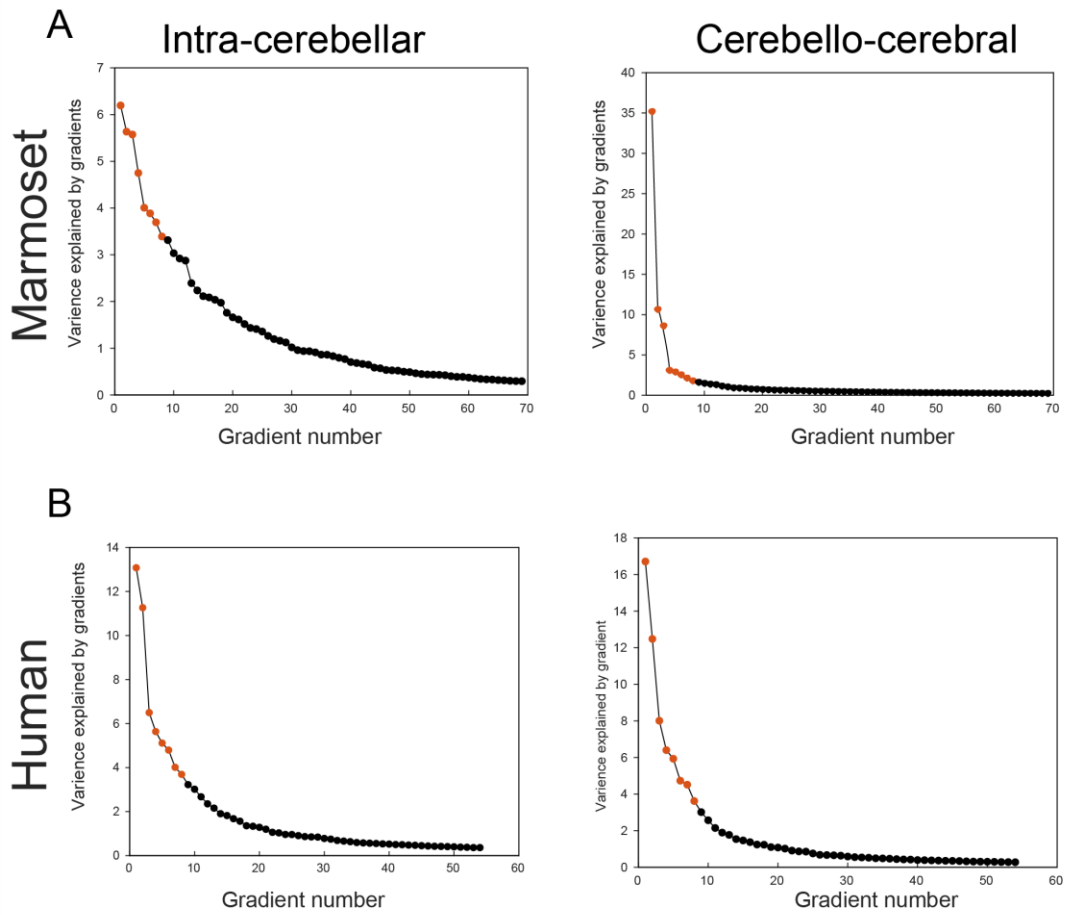

Figure S1. The percentages of variances explained by the gradients of the intra-cerebral connectivity and the cerebello-cerebral connectivity in marmosets (**A**) and humans (**B**), respectively.

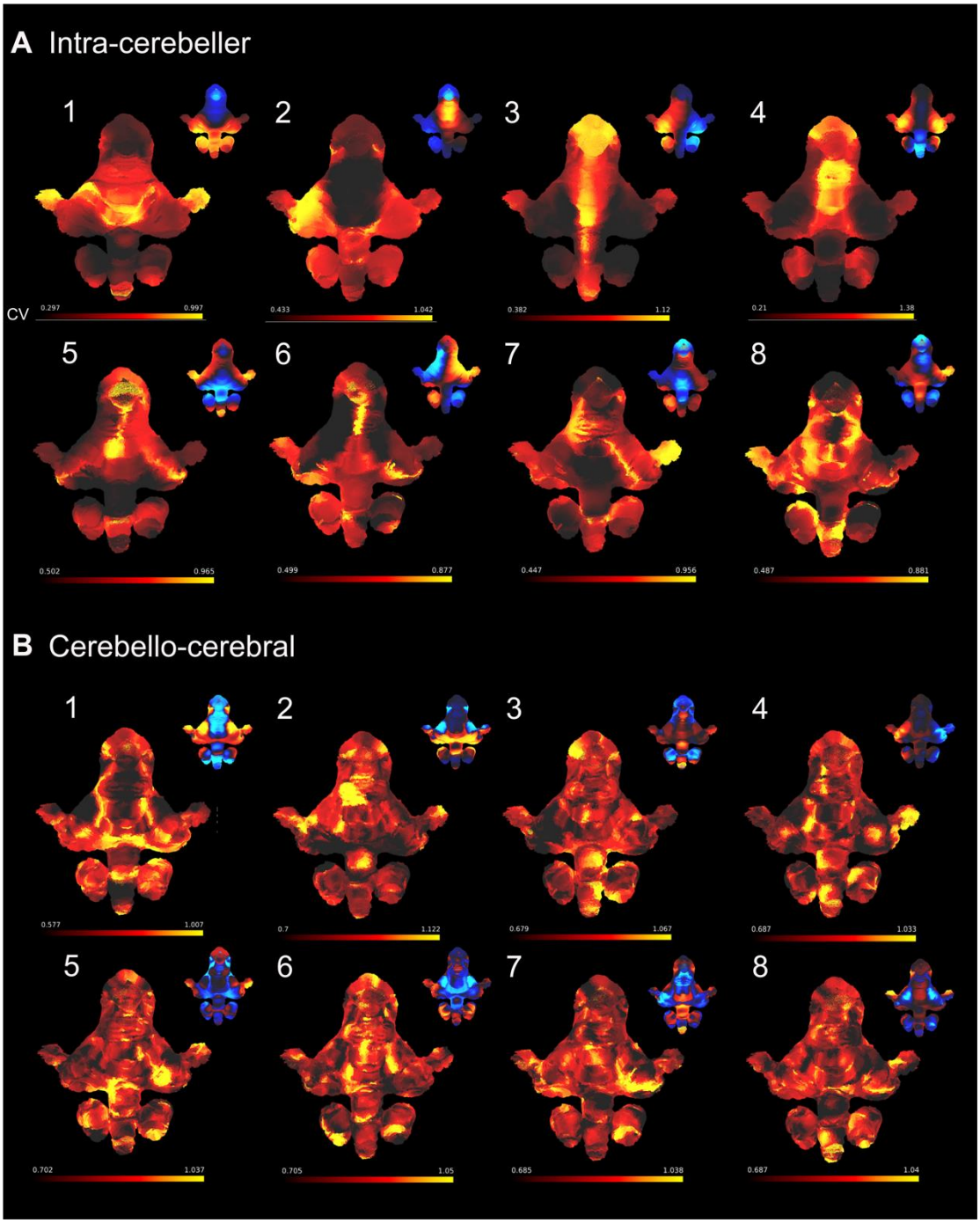

Figure S2. The individual variability of gradients 1 to 8 for the intra-cerebellar connectivity (**A**) and the cerebello-cerebral connectivity (**B**). The gradient itself is also displayed on the right corner of each panel. CV: coefficients of variability.

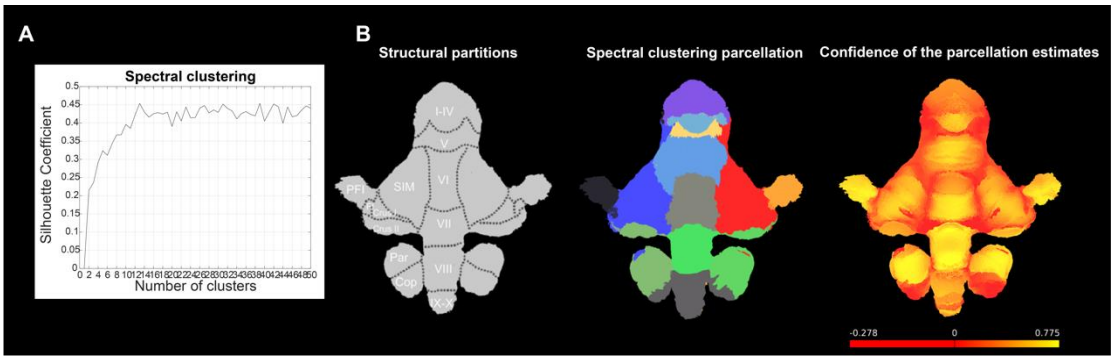

Figure S3. The parcellation results of the cerebellar cortex based on the spectral clustering on the intra-cerebellar functional connectivity. (**A**) Silhouette coefficient suggests that K = 13 is the optimal option. (**B**) The clustering results (depicted in the middle panel) exhibit similarity with the anatomical subdivisions of the cerebellum (left panel). Specifically, the vermis is clearly distinguished from the hemispheres, and the lobules I-IV (motor areas) are roughly grouped into a single cluster. The PFL and Crus II regions are clearly separated out. Furthermore, the population confidence of the parcellation, based on 39 animals, suggests that regions situated near parcellation boundaries are less certain while the center regions are more confident (right panel).

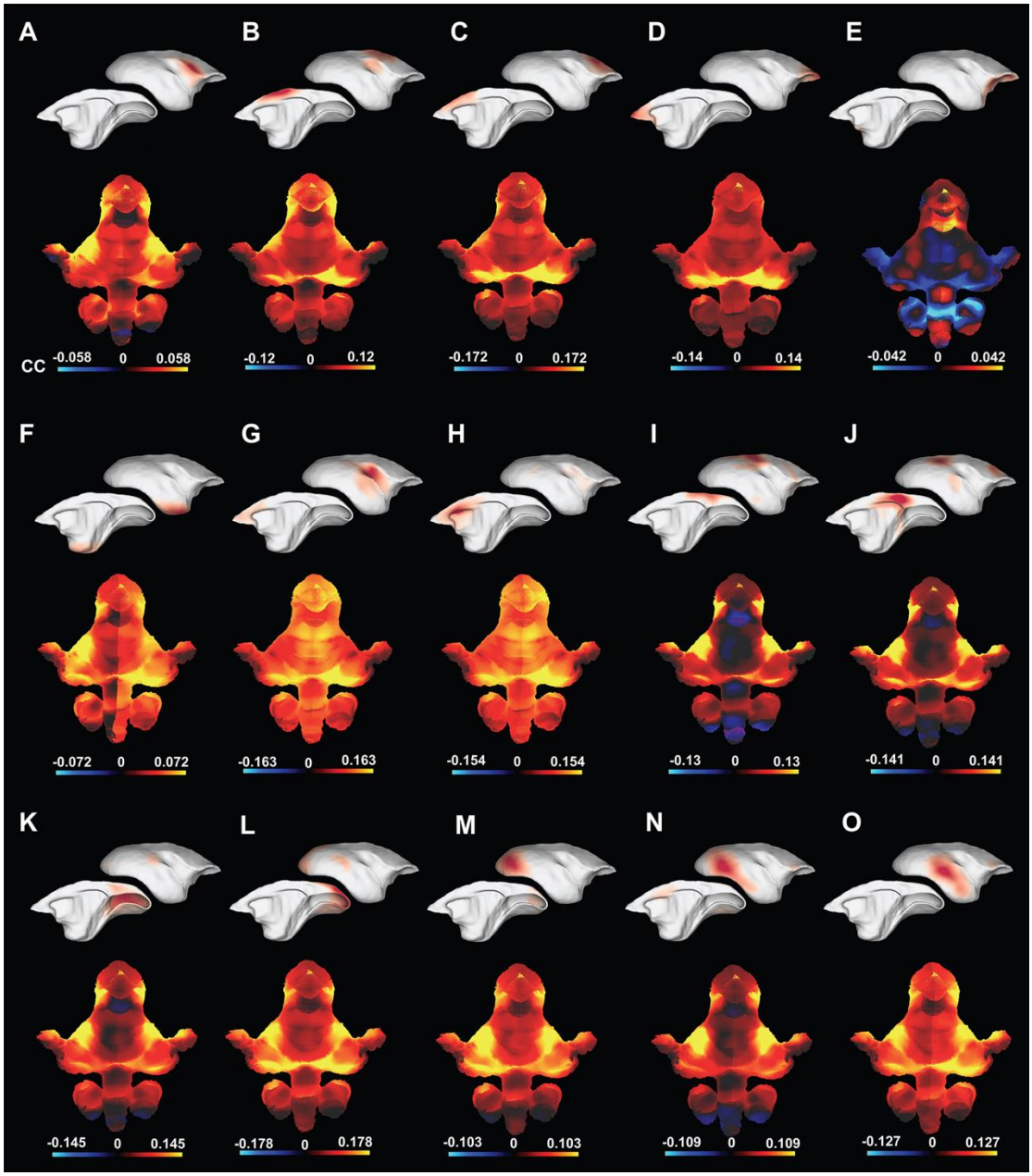

Figure S4. Functional connectivity patterns between the cerebral functional networks and the cerebellar cortex, including (**A**) the ventral somatomotor, (**B**) the dorsal somatomotor, (**C**) the premotor, (**D**) the frontal pole, (**E**) the orbital frontal cortex, (**F**) the parahippocampus and temporal pole, (**G-H**) the auditory and salience-related network, (**I-J**) two trans-modal networks, including a putative frontoparietal network and the default-mode-network, and (**K-O**) visual-related networks from the primary visual cortex to higher-order functional regions. CC: correlation coefficients.

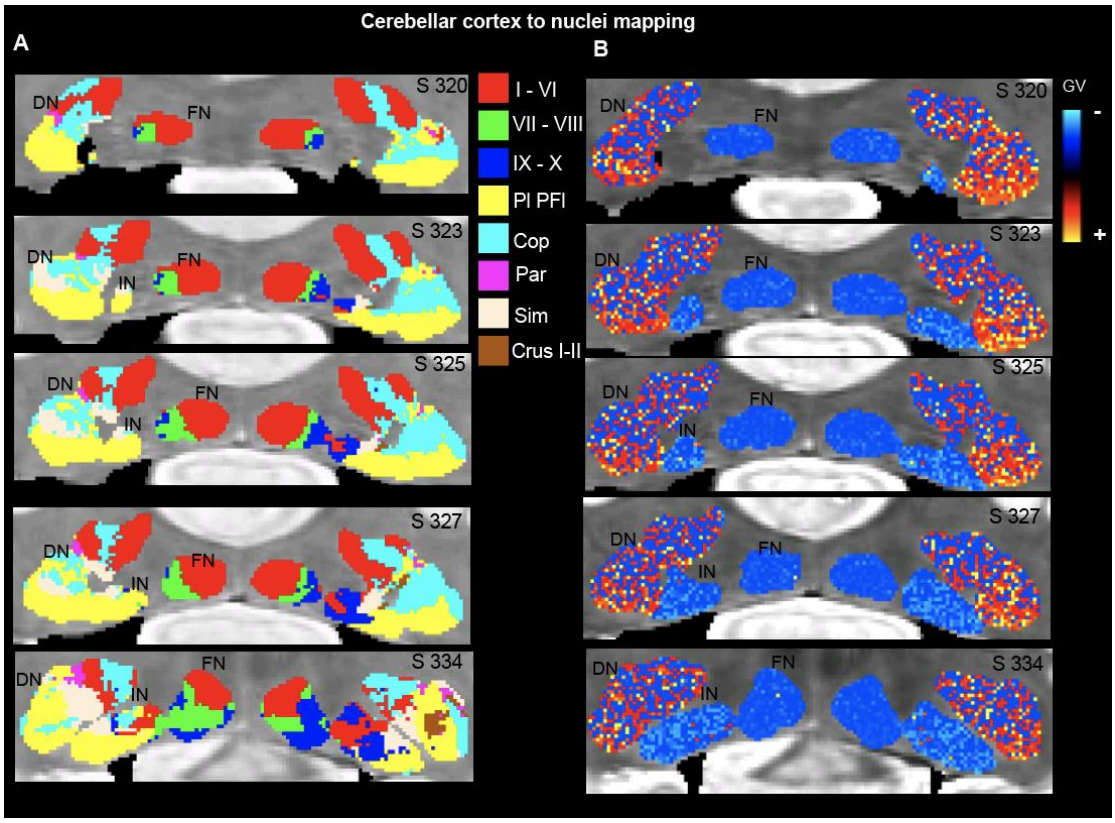

Figure S5. Mapping the properties of the cerebellar cortex to the nuclei based on their structural connectivity using 80 μm isotropic data. The left shows the cerebellar-lobule labels mapped (**A**), and the right is the cerebello-cerebral functional gradient-1 mapped on the nuclei (**B**). For each panel, the coronal slices 320,323,325,327 and 334 are shown from top to bottom. GV: gradient value.

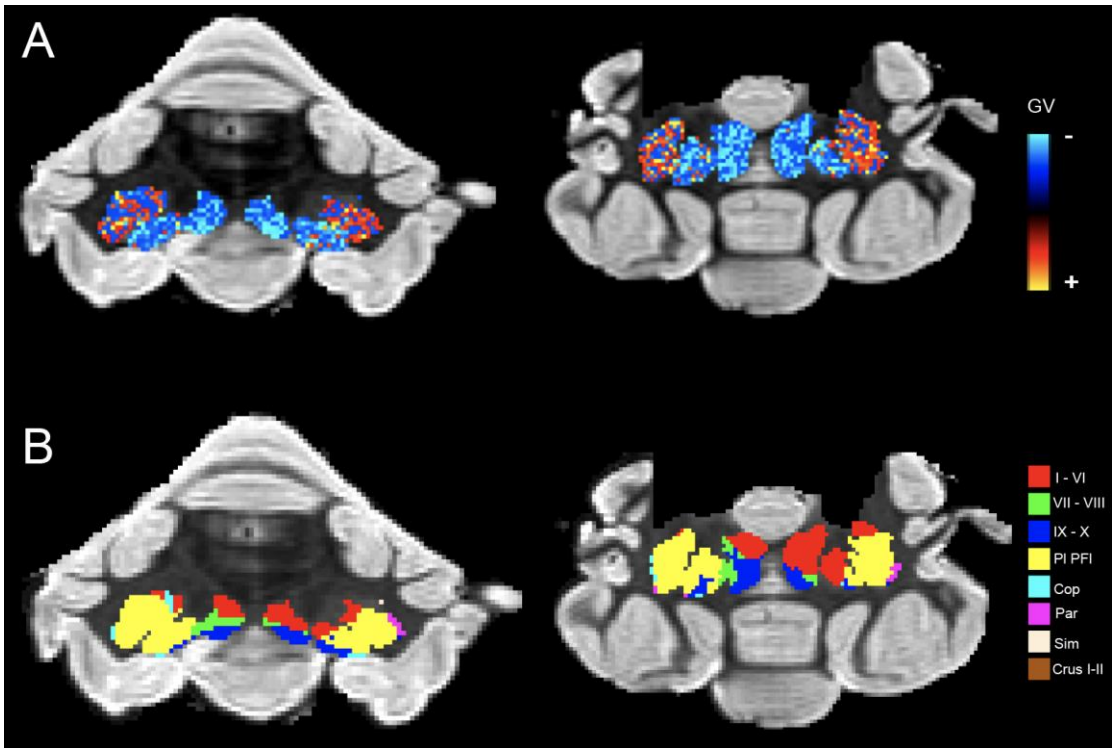

Figure S6. Mapping the properties of the cerebellar cortex to the nuclei based on their structural connectivity using 150 µm isotropic data. (**A**) The cerebello-cerebral functional gradient-1 is mapped on the nuclei. GV: gradient value. (**B**) The cerebellar-lobule labels are mapped on the nuclei.

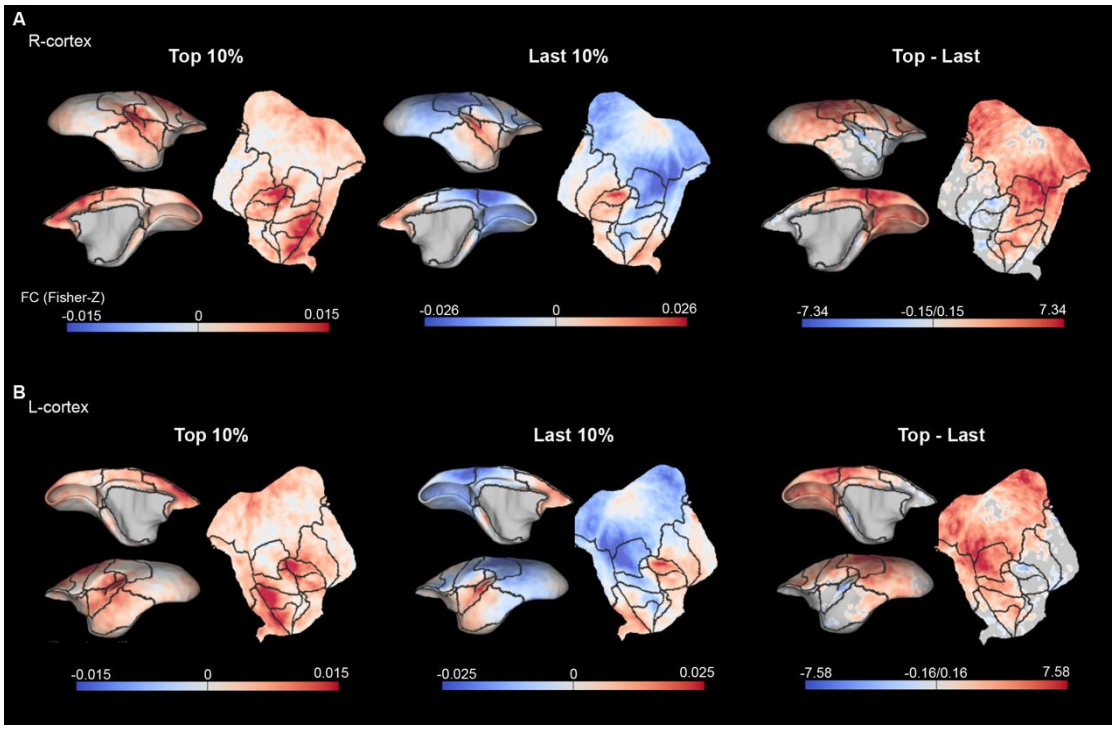

Figure S7. Functional connectivity patterns of two extremes (top 10 % and last 10% value of the nuclei-neocortex gradient-1) to the right cerebral cortex (A) and the left cortex (B) and their statistical difference by paired t-test ($p<0.05$, FDR corrected). FC: Fisher-z transformed functional connectivity.